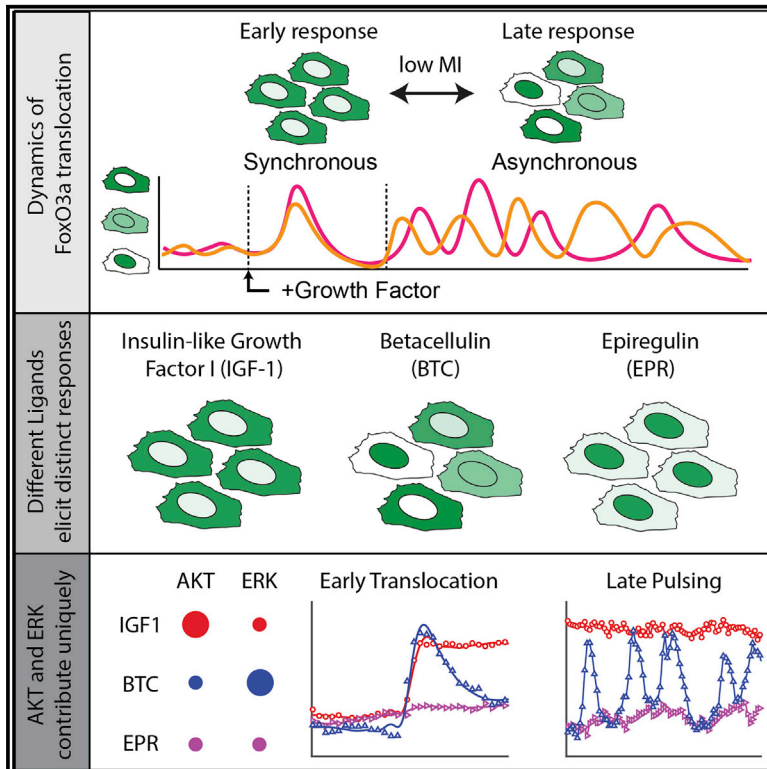


## Encoding Growth Factor Identity in the Temporal Dynamics of FOXO3 under the Combinatorial Control of ERK and AKT Kinases

### Graphical Abstract



### Authors

Somponnat Sampattavanich, Bernhard Steiert, Bernhard A. Kramer, Benjamin M. Gyori, John G. Albeck, Peter K. Sorger

### Correspondence

somponnat.sam@mahidol.edu (S.S.), peter\_sorger@hms.harvard.edu (P.K.S.)

### In Brief

Eukaryotic transcription factors frequently oscillate between the nucleus and cytosol. We show that translocation by human FOXO3 is pulsatile rather than oscillatory and subject to combinatorial control by the ERK and Akt pathways. As a result, FOXO3 dynamics can encode the identities and concentrations of diverse extracellular growth factors.

### Highlights

- Ligand-stimulated FOXO3 nuclear-cytosolic shuttling is pulsatile, not oscillatory
- FOXO3 dynamics can encode growth factor identities and concentrations
- FOXO3 dynamics are under combinatorial control by the ERK and Akt pathways
- Diversity of FOXO3 dynamics is lost in cells with ERK and AKT pathway mutations



# Encoding Growth Factor Identity in the Temporal Dynamics of FOXO3 under the Combinatorial Control of ERK and AKT Kinases

Somponnat Sampattavanich,<sup>1,2,\*</sup> Bernhard Steiert,<sup>1,3,4</sup> Bernhard A. Kramer,<sup>1,5</sup> Benjamin M. Gyori,<sup>1</sup> John G. Albeck,<sup>6</sup> and Peter K. Sorger<sup>1,7,\*</sup>

<sup>1</sup>HMS LINC Center and Laboratory of Systems Pharmacology, Department of Systems Biology, Harvard Medical School, WAB Room 438, 200 Longwood Avenue, Boston, MA 02115, USA

<sup>2</sup>Siriraj Laboratory for Systems Pharmacology, Department of Pharmacology, Faculty of Medicine Siriraj Hospital, Mahidol University, 12th Floor Srisavarindhira Building, 2 Wanglang Road, Bangkoknoi, Bangkok 10700, Thailand

<sup>3</sup>Institute of Physics, University of Freiburg, Freiburg, Germany

<sup>4</sup>Freiburg Center for Systems Biology, University of Freiburg, Freiburg, Germany

<sup>5</sup>Division of Systems Biology of Signal Transduction, German Cancer Research Center, Heidelberg, Germany

<sup>6</sup>Department of Molecular and Cellular Biology, University of California, Davis, Davis, CA, USA

<sup>7</sup>Lead Contact

\*Correspondence: [somponnat.sam@mahidol.edu](mailto:somponnat.sam@mahidol.edu) (S.S.), [peter\\_sorger@hms.harvard.edu](mailto:peter_sorger@hms.harvard.edu) (P.K.S.)

<https://doi.org/10.1016/j.cels.2018.05.004>

## SUMMARY

Extracellular growth factors signal to transcription factors via a limited number of cytoplasmic kinase cascades. It remains unclear how such cascades encode ligand identities and concentrations. In this paper, we use live-cell imaging and statistical modeling to study FOXO3, a transcription factor regulating diverse aspects of cellular physiology that is under combinatorial control. We show that FOXO3 nuclear-to-cytosolic translocation has two temporally distinct phases varying in magnitude with growth factor identity and cell type. These phases comprise synchronous translocation soon after ligand addition followed by an extended back-and-forth shuttling; this shuttling is pulsatile and does not have a characteristic frequency, unlike a simple oscillator. Early and late dynamics are differentially regulated by Akt and ERK and have low mutual information, potentially allowing the two phases to encode different information. In cancer cells in which ERK and Akt are dysregulated by oncogenic mutation, the diversity of states is lower.

## INTRODUCTION

Activation of different growth factor receptors induces distinct phenotypes and cellular responses while engaging a common set of kinase cascades. The Ras/ERK and PI3K/Akt kinase cascades are particularly important in linking transmembrane receptor activity to mitogenic transcription and cell cycle progression. It remains unclear how cells transduce information about receptor occupancy to transcription factors using a limited number of overlapping signal transduction molecules. Some studies suggest that the identity of growth factors is encoded in the dy-

namics of effector activation (Traverse et al., 1994) or differential activation of ERK and Akt pathways (Chen et al., 2012). Theoretical studies predict that activation of parallel signaling pathways might serve to increase the accuracy of signaling downstream of a receptor input (Cheong et al., 2011).

Signaling kinases and the transcription factors they control often switch between on and off states repeatedly over the course of a 12- to 24-hr response (Levine et al., 2013; Purvis and Lahav, 2013). Such switching is frequently asynchronous from one cell to the next and best monitored using time-lapse microscopy of fluorescent reporter proteins. Both TP53 and nuclear factor (NF)- $\kappa$ B undergo nuclear/cytosolic translocation in which the duration of the active (nuclear) state determines promoter selectivity and level of transcription. TP53 activation by DNA damage was initially thought to involve a few strongly damped oscillations (Lev Bar-Or et al., 2000) but live-cell imaging reveals extended asynchronous oscillation at a single-cell level (Batchelor et al., 2011; Lahav et al., 2004). Similar long-duration pulsing has been observed for NF- $\kappa$ B following exposure of cells to inflammatory cytokines such as tumor necrosis factor alpha (Nelson et al., 2004; Tay et al., 2010).

Pulsing genetic circuits have the potential to encode information in pulse amplitudes, frequencies, and duration (Levine et al., 2013). For example, the activity of the extracellular signal regulated kinase ERK, the downstream effector of the mitogen-activated protein kinase (MAPK or MEK/ERK) cascade, is pulsatile when cells are exposed to low concentrations of growth factor. The likelihood that a cell will enter S phase correlates with the duration of the ERK<sub>ON</sub> state (Albeck et al., 2013). The regulation and coding potential of pulsatile circuits is best understood in single-cell organisms. In yeast, both frequency-modulated (FM) and amplitude-modulated (AM) encoding has been observed for Msn2, a transcription factor involved in general stress response, and the identity and intensity of upstream activators appears to be encoded by FM and AM processes working in tandem (Hansen and O'Shea, 2015). Combinatorial gene regulation is achieved by modulating the relative timing of Msn2 and Mig1 pulses (Mig1 is a transcriptional repressor that controls



metabolic genes) (Lin et al., 2015). Eukaryotic cells have long been known to exploit combinatorial transcriptional control but the role of pulsing circuits in such control has only recently become a topic of interest.

The Forkhead box O3 transcription factor (FOXO3) functions as an integrative node for several upstream signaling networks. In mammalian cells, FOXO3 is one of four FoxO family-member proteins implicated in biological processes that include cycle arrest, apoptosis, oxidative stress, cell migration, and cell metabolism. Combinations of upstream inputs alter the post-translational modification state of FOXO3 and these changes control abundance, subcellular localization, and DNA binding capacity (Calnan and Brunet, 2008; Eijkelenboom and Burgering, 2013). Mitogenic growth factors negatively regulate FOXO3 activity via the MEK/ERK and the PI3K/Akt kinase cascades (Biggs et al., 1999; Brunet et al., 1999; Yang et al., 2008), whereas oxidative stress exerts positive regulation via the JNK and MST1 kinases (Essers et al., 2004; Lehtinen et al., 2006).

Phosphorylation of FOXO3 by Akt at T32, S253, and S315 promotes interaction with 14-3-3 proteins, causing nuclear-to-cytosolic translocation and relieving repression of mitogenic genes (Brunet et al., 2002). ERK phosphorylation on S294, S344, and S425 also promotes FOXO3 nuclear-to-cytosolic translocation and degradation via MDM2-dependent ubiquitin-mediated proteolysis (Yang et al., 2008). Other regulators of FOXO3 activity include energy stress via the AMPK pathway (Greer et al., 2007), genotoxic stress via CDK proteins (Huang et al., 2006), and cytokines via the I $\kappa$ B kinase (Hu et al., 2004). Measuring and analyzing such complex signal encoding is fundamental to understanding combinatorial control by FoxO family transcription factors and may be of diagnostic value in cell types with misregulated FoxO proteins (van der Horst and Burgering, 2007).

In this article, we study how the identities and concentrations of growth factors are encoded in the dynamics of FOXO3 activity. We find that FOXO3 exhibits complex patterns of nuclear-to-cytosolic translocation in ligand-activated cells on multiple time scales. Across all cells in a population, synchronous cytosolic translocation is observed within 20 min of ligand addition, followed by a return to the nucleus and then an extended period of asynchronous (and non-oscillatory) shuffling between cytosolic and nuclear compartments. The relative magnitude of synchronous translocation and pulsing varies with the identity of the activating growth factor and the properties of the cell line with synchronous translocation regulated primarily by Akt and pulsing by Akt plus ERK. Our data provide insight into combinatorial control of FOXO3 by immediate-early signal transduction cascades pathways and demonstrate how a single transcription factor can assume a wide range of possible states in response to different upstream inputs.

## RESULTS

### Design and Characterization of the F3aN400-Venus Reporter

FoxO localization has been studied in live mammalian cells using fluorescent protein fusions (Gross and Rotwein, 2015; Senapedis et al., 2011), but the impact of differences in ligand identity and concentration has not been investigated in depth. We therefore constructed a FOXO3 translocation reporter responsive to

both ERK and Akt that is not expected to perturb normal transcription (Figure 1A). A Venus fluorescent protein was fused to a 400-residue domain of human FOXO3 containing all three known sites of Akt phosphorylation (T32, S253, and S315; Figure 1A, green text) and two of three known ERK phosphorylation sites (S294 and S344; blue text) but lacking a transactivation domain. The F3aN400-Venus reporter also carried an H212R loss-of-function mutation in the DNA binding domain to prevent dominant-negative effects on endogenous FOXO3 (Tran et al., 2002); such effects were observed with a full-length FOXO3 construct. To determine if F3aN400-Venus faithfully captures FOXO3 dynamics, parallel cultures of parental and F3aN400-Venus expressing 184A1 cells were treated with epidermal growth factor (EGF) at concentrations from near physiological to saturating (0.4–100 ng/mL) in combination with the allosteric Akt1/2/3 inhibitor MK-2206 at varying doses; this protocol was observed to elicit a wide range of FOXO3 states from fully nuclear localized to fully cytosolic (Figure 1B). F3aN400-Venus was imaged directly and parental cells stained with anti-FOXO3 antibody. When cells were segmented and the median nuclear-cytoplasmic translocation value (median of  $\log_{10}[C_{\text{norm}}/N_{\text{norm}}]$ ) compared for the reporter and endogenous protein, a Pearson's correlation coefficient of 0.91 was obtained, representing a high degree of concordance. The dynamic range estimated for the nuclear-cytoplasmic ratio was similar for endogenous FOXO3 (–0.8 to 0; Figure 1B), and F3aN400-Venus (–0.6 to 0.2); as expected, dynamic range varied depending on how background intensity was computed but values were insensitive to the image segmentation algorithm used (see STAR Methods for complete definitions; Figures S1A–S1D). We conclude that the localization of the F3aN400-Venus report and endogenous FOXO3 are similar across a wide range of conditions.

Variability in cytoplasmic-to-nuclear ratio across cells in a culture (as quantified by interquartile range; IQR), serves as a surrogate measurement for shuttling between the nucleus and cytoplasm in the absence of a reporter (this makes the ergodic assumption that difference across many cells at a single point in time are reflective of differences over time in a single cell; Figure S1E). Across a range of conditions, the median and IQR of the cytoplasmic/nuclear ratio for endogenous FOXO3 and the F3aN400-Venus reporter were similar, suggesting that the fluorescent sensor recapitulates most but not all of the dynamics of endogenous FOXO3 (Figure S1F). The largest discrepancy was observed at low levels of cytoplasmic translocation when the endogenous protein is expected to be more completely retained in the nucleus than the reporter because only the former is active in DNA binding. In common with many live-cell studies of transcription factor shuttling, we were unable to distinguish the behavior of FOXO3 that is chromatin bound and FOXO3 that is free in the nucleus. Nonetheless, F3aN400-Venus appears to be a faithful reporter of overall FOXO3 state.

To investigate regulation of F3aN400-Venus by Akt and ERK, serum-starved 184A1 cells were treated with one of six growth factors at 100 ng/mL and the levels of phosphorylated pAkt<sup>S473</sup> and pERK<sup>T202/Y204</sup> measured by immunoblotting (phosphorylation at these sites, henceforth pERK and pAkt, is a surrogate for Akt and ERK kinase activity; Figure S1G). Insulin growth factor (IGF)1 caused strong and persistent Akt activation, whereas

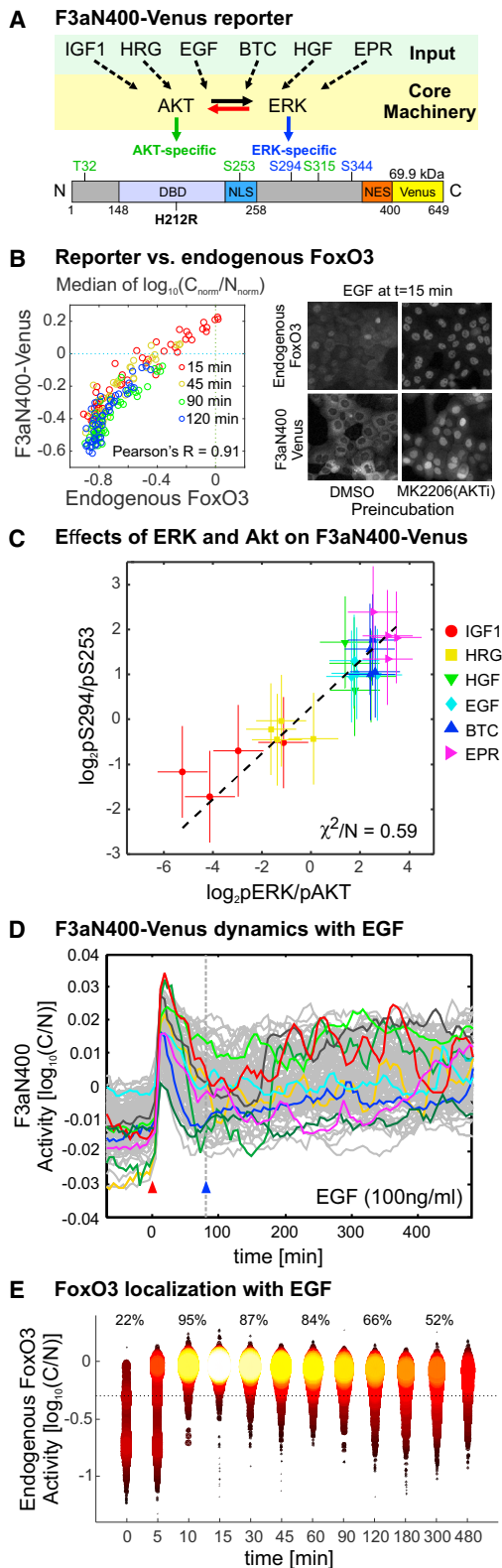


**Figure 1. Design and Characterization of the F3aN400 Reporter with Growth Factor Stimulation**

For a Figure360 author presentation of Figure 1, see the figure legend at <http://dx.doi.org/10.1016/j.cels.2018.05.004#mmc4>.

EGF, betacellulin (BTC), epiregulin (EPR), hepatocyte growth factor (HGF), and heregulin (HRG) caused transient activation. The opposite pattern was observed for ERK, with EGF eliciting the strongest ERK activity and IGF1 the least. These differences corresponded well to phosphorylation of F3aN400-Venus, as measured by pS294 and pS253 ratios 15–480 min after growth factor addition (Figures 1C and S1G). Use of selective kinase inhibitors (MK-2206 for Akt1/2/3 and CI-1040 for MEK1/2) confirmed that F3aN400-Venus phosphorylation was ERK-dependent on S294 and Akt-dependent on S253 (Figure S1G; right-most immunoblot panel), consistent with the well-established biology of FOXO3 (Brunet et al., 2001; Yang et al., 2008). We conclude that the F3aN400-Venus reporter recapitulates previously described patterns of FOXO3 nuclear translocation and phosphorylation.

To study F3aN400-Venus translocation dynamics in response to growth factors, F3aN400-Venus localization was monitored by live-cell microscopy over a 24-hr period. Following exposure to EGF (Figure 1D, red arrowhead), synchronous cytosolic translocation of the reporter was observed in all cells, peaking at t = 15–20 min, followed by a return to the nucleus by t = 60–100 min. Starting at ~80 min after EGF addition (Figure 1D, blue arrowhead), shuttling between the cytosol and nucleus was observed every 50–100 min. Shuttling was not observed in all cells but, when it did occur, continued for up to 24 hr and was asynchronous from one cell to the next. Immunofluorescence imaging of endogenous FOXO3 in >1,000 fixed cells at each time point confirmed translocation from the nucleus to the cytosol in >90% of cells at 10–30 min after EGF addition

(A) Schematic of the F3aN400-Venus reporter and its upstream activators. mVenus Fluorescent Protein was fused to residues 1–400 of native human FOXO3, which contained Akt-dependent T32, S253, and S315 (green) and ERK-dependent S294 and S344 (blue) phosphorylation sites but lacked the transactivation domain. An H212R mutation inactivated FOXO3 binding and prevented dominant-negative effects on endogenous FOXO3.

(B) Comparison of endogenous FOXO3 and F3aN400-Venus localization. Parental and reporter-expressing cells 184A1 cells were pre-treated with Akt1/2/3 inhibitor (MK2206; at eight doses from 0 to 1  $\mu$ M) for 1 hr prior to EGF stimulation (at six doses from 0.4 to 100 ng/mL). Parental cells were immunostained with anti-FOXO3 antibody and reporter-expressing cells imaged directly. Data were collected at 15 (red datapoints), 45 (yellow), 90 (green), and 120 (blue) min. Each datapoint represents the median of translocation, calculated from  $\log_{10}$  of the normalized cytoplasmic/nuclear intensity ratio ( $C_{norm}/N_{norm}$ ). Right panels show example images for both types of cells treated with DMSO or MK2206 (at 1  $\mu$ M) prior to EGF stimulation (100 ng/mL).

(C) Relationship between the  $pERK^{T202/Y204}$ -to- $pAkt^{S473}$  phosphorylation ratio, a surrogate for relative ERK and Akt activity and the relative phosphorylation of the reporter (the  $pF3aN400^{S294}$ -Venus to  $pF3aN400^{S253}$ -Venus ratio) in cells exposed to 100 ng/mL growth factor at four time points from 15 to 480 min. Error bars represent propagated errors from two biological replicates (see STAR Methods for complete details). Also refer to Figure S1G and Table S1 for complete dataset.

(D) Single-cell trajectories of F3aN400-Venus translocation in 184A1 cells imaged every 5 min following exposure to 100 ng/mL EGF. Red arrowhead marks the time of ligand addition (t = 0). Ten randomly selected of ~100 total trajectories are highlighted in color. Blue arrowhead at t = 80 min denotes end of synchronous translocation.

(E) Density plots (>1000 cells per time point) showing the localization of endogenous FOXO3 based on immunostaining at different times after 100 ng/mL EGF addition. Percentages of cells with  $\log_{10}(C/N)$  above the cutoff (dotted line) are shown above.

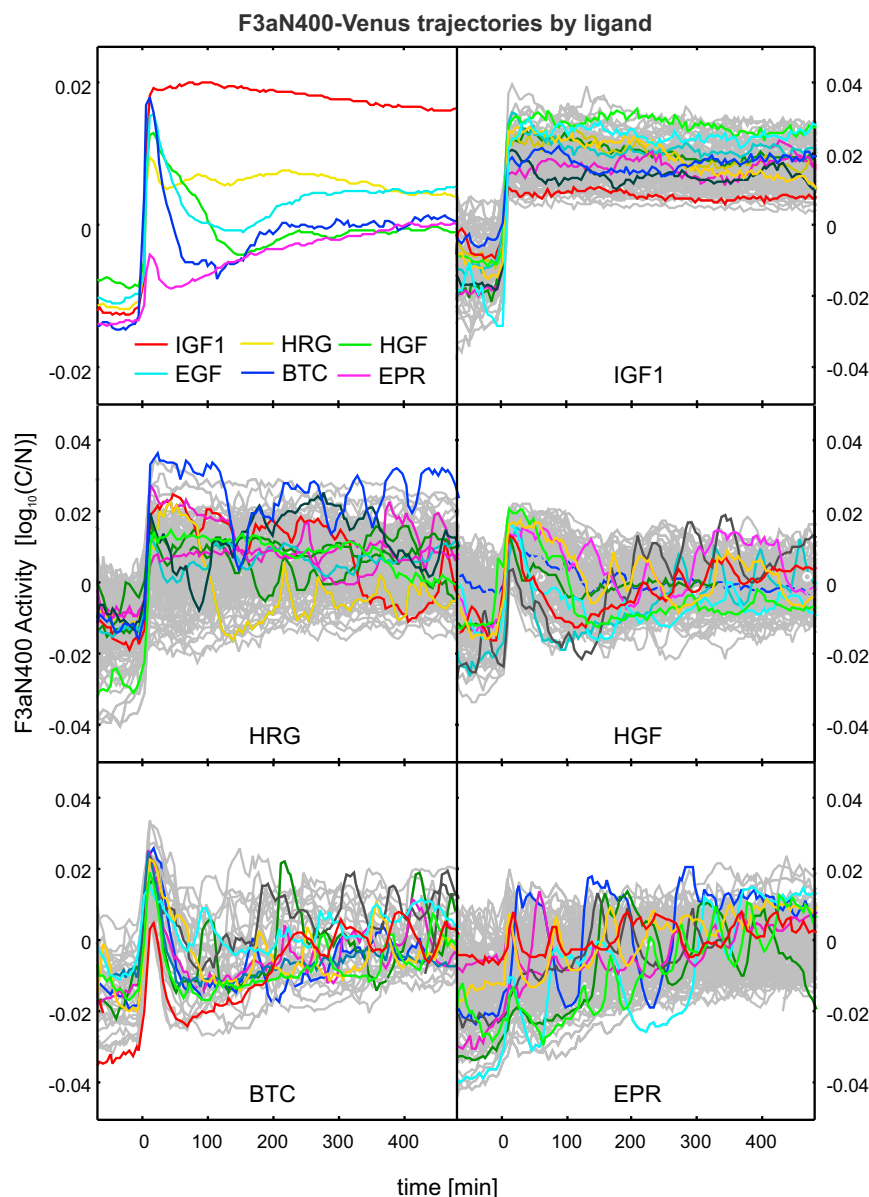


**Figure 2. Growth Factor Stimulated Dynamics of F3aN400-Venus Translocation**

F3aN400-Venus translocation dynamics following exposure of 184A1 cells to IGF1, HRG, HGF, BTC, and EPR at 100 ng/mL. Top-left panel depicts the average of >100 trajectories per ligand and other panels show single-cell trajectories; ten randomly selected trajectories are highlighted in color.

(Figure 1E), followed by a progressive increase in the IQR of  $\log_{10}(C/N)$  after 30 min, consistent with live-cell studies. When 184A1 cells were exposed to one of six growth factors at concentrations ranging from roughly physiological to saturating, we found that IGF1 elicited sustained nuclear-to-cytoplasmic translocation while the EGF-like growth factors BTC and EPR elicited transient translocation followed by varying degrees of pulsing (Figure 2; see also Movie S1). Thus, FOXO3 translocation exhibits qualitatively distinct translocation dynamics depending on growth factor.

### Synchronous FOXO3 Translocation Dynamics Vary with Growth Factor Dose and Identity

To quantify differences in F3aN400 trajectories following growth factor stimulation of 184A1 cells, >100 trajectories were collected per condition and then separated into early synchro-

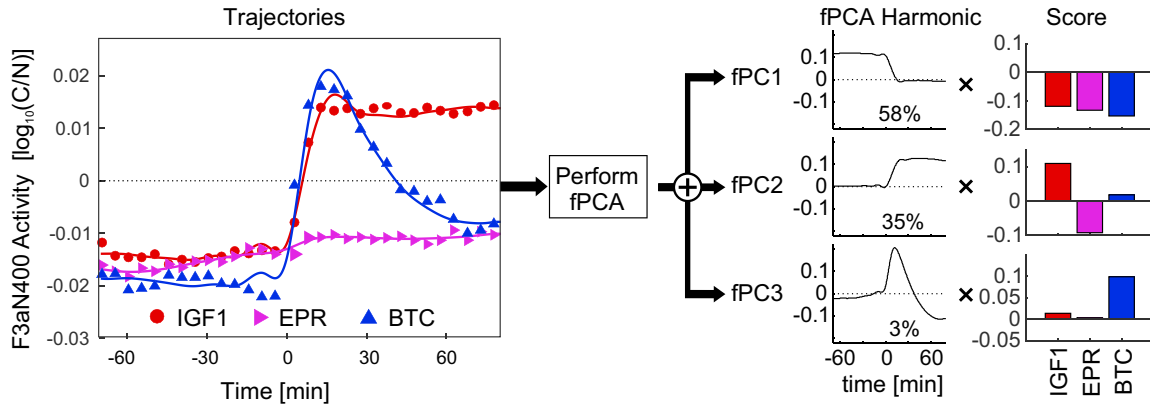
nous and late pulsing phases. For the early synchronous phase, functional principal component analysis (fPCA) was used to decompose the signal prior to and immediately after ligand addition ( $t = -70$  to  $+80$  min) into a weighted set of orthogonal harmonic functions. Three harmonic functions explained >95% of variance across growth factors and doses, representing excellent performance for a PCA model (Figures 3A and S2A). The harmonic corresponding to the first principal component (fPC1) comprised the pre-treatment baseline signal, while fPC2 corresponded to a rapid increase in cytoplasmic-nuclear ratio to a high and constant value by  $t = 20$  min; fPC3 was transient, rising rapidly to a maximum at  $t = 15$  min and then falling below baseline levels by 60 min (Figure 3A). In the landscape of fPC2 versus fPC3, BTC, IGF1, and EPR represented extrema: BTC scored relatively high in both fPC2 and fPC3, IGF1 scored high in fPC2, and EPR scored low in both fPC2 and fPC3 (Figure 3B). These differences were statistically significant, but other ligands exhibited intermediate behavior and could not be as cleanly distinguished from each other (Figure 3C). For all but IGF1, fPC2 and fPC3 scores varied smoothly with dose (Figure 3D) suggesting that differences in loadings

reflect qualitative differences among ligands and not simply varying degrees of receptor activation. Scores for fPC1 were variable and not significantly different among growth factors, whereas fPC2 and fPC3 scores discriminated among ligands with high confidence (Figure S2B;  $p < 10^{-10}$  based on Wilcoxon rank-sum test as compared with unstimulated cells). We conclude that different growth factors induce significantly different FOXO3 translocation dynamics in the initial synchronous phase of response to growth factor.

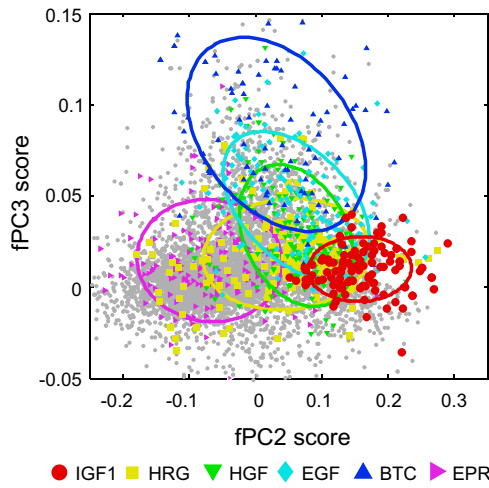
### FOXO3 Translocation Is Pulsatile but Not Oscillatory

When harmonics comprising fPC1–fPC5 were added together in proportion to their scores, the contribution of long-wavelength changes to F3aN400-Venus dynamics could be visualized (Figure 3E). In the case of EGF we found that this “trend” response comprised both synchronous translocation into the cytoplasm

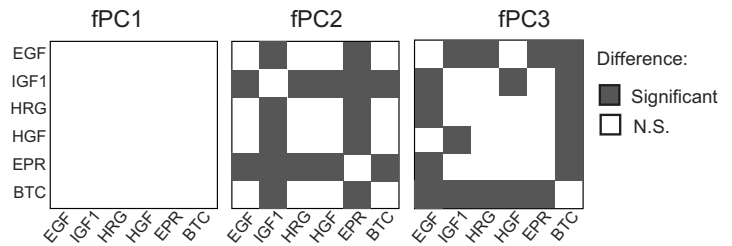
**A Decomposing early trajectories by fPCA**



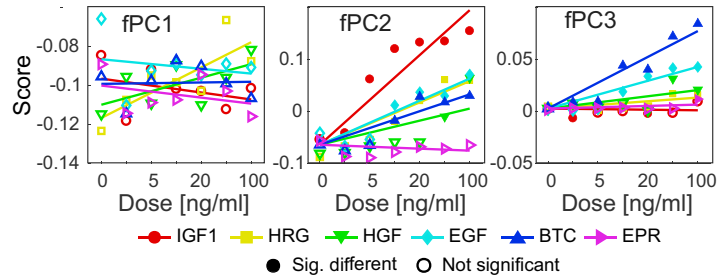
**B Scores plot fPC2 vs fPC3**



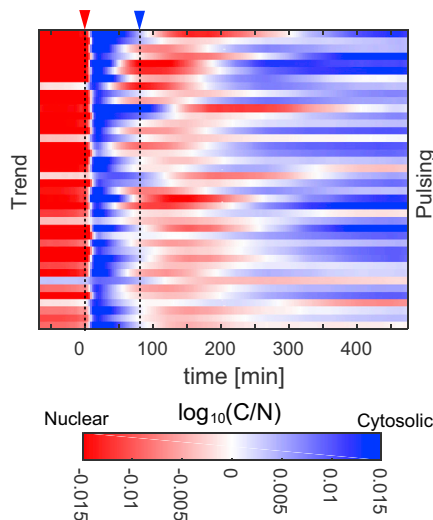
**C Pairwise comparison of fPCA scores by ligand**



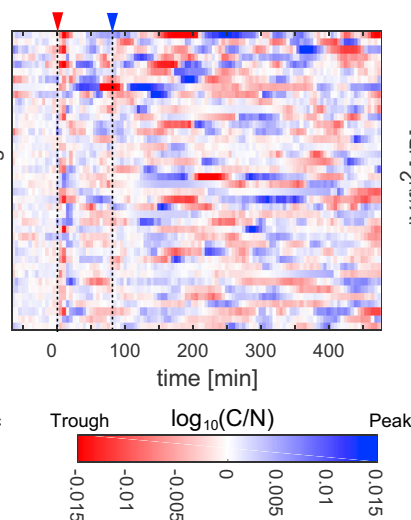
**D fPCA scores for various ligand identity and dosing**



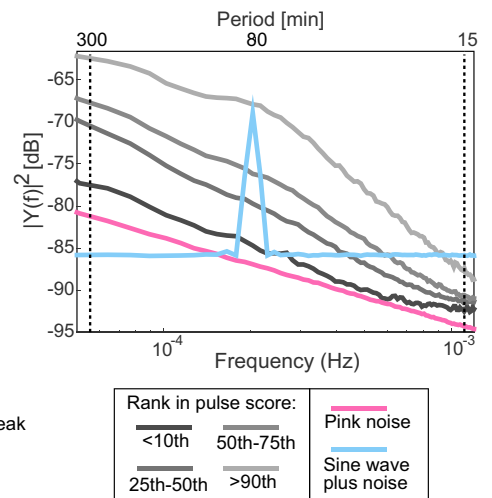
**E EGF: fPC1-5 combined**



**E EGF: pulsing**



**F Frequency Density Spectrum**



(legend on next page)

and quick return to the nucleus by  $t = 80$  min (as described above), as well as gradual return to the cytosol between  $t = 200$  and  $300$  min in a majority of cells (Figure 3E, left panel). Subtracting this trend response from the original trajectories revealed the pulsatile signal (Figure 3E, right panel). When fPCA analysis was performed on trajectories between  $t = 80$  and  $1,580$  min, the PCA scores were significantly different from those of unstimulated cells only in the case of IGF1. Thus, only IGF1 is associated with a significant “trend” response at later times, consistent with manual inspection showing sustained cytosolic FOXO3 localization. For other ligands, fPCA scores for the late response were insignificantly different from each other and from untreated cells. Reconstructed late-phase trend lines obtained by adding these fPCA harmonics together (Figure S3A) were nonetheless useful in correcting for drift and background fluorescence on a trajectory-by-trajectory basis.

Oscillation is often observed in dynamic systems having strong feedback regulation (Elowitz and Leibler, 2000; Lahav et al., 2004). A key characteristic of oscillatory systems is stability in the frequency domain (Halford et al., 1973), a property that can be evaluated by computing spectral density, the distribution of power versus frequency. A purely sinusoidal oscillator, when sampled in discrete time, gives rise to a narrow spectral density distribution whose width varies with sampling error and signal-to-noise ratio (the blue line in Figure 3F represents an oscillator with a frequency of  $\sim 0.2$  mHz sampled every 5 min convolved by measurement noise). However, detrended trajectories for F3aN400-Venus exhibited an inverse relationship between power and frequency in the range of  $0.05$ – $2$  mHz (Figure 3F); this was true when the data were analyzed either in aggregate or ligand-by-ligand. Such a relationship is a characteristic of  $1/f$  or “pink” noise (where  $f$  is frequency), observed in many non-equilibrium physical systems (Hausdorff and Peng, 1996). When the power spectrum was computed for trajectories with the greatest degree of pulsing (see below), we observed a statistically significant deviation from pure  $1/f$  behavior at  $\sim 0.2$  mHz, which corresponds to a wavelength of  $80 \pm 30$  min. This accounts for the apparent periodicity of some F3aN400-Venus trajectories. We conclude that the pulsatile component of F3aN400-Venus trajectories is not oscillatory in the conventional sense, although it does have weak periodicity. Irregular pulsing is a feature of both stochastic and chaotic dynamical systems and either or both could be involved in F3aN400-Venus dynamics (Timmer et al., 2000).

### FOXO3 Pulsing Varies with Ligand and Carries Distinct Information

Because F3aN400-Venus trajectories were not oscillatory, we quantified shuttling using a “pulse score” schematized in Figure 4A (and described in full in STAR Methods). This score comprised a nonlinear combination of (1) the number of pulses, (2) the pulse amplitude, (3) the signal-to-noise ratio in the images, (4) the average peak duration, and (5) the average peak-to-peak distance. We quantified the fraction of pulsing cells in different conditions using a threshold of  $\sim 0.6$  in pulse score, which optimally discriminated trajectories in cells exposed to BTC and IGF1 (the least and the most pulsatile trajectories as judged by the human eye; Figure 4A). We found that the fraction of pulsing cells rather than pulse amplitude or duration varied the most between conditions, justifying our use of discretization (Figures 4B and S3B). Approximately 10% of serum-starved 184A1 cells exhibited pulsing in the absence of growth factor (Figure 4B; “0 ng/mL”); addition of IGF1 suppressed baseline pulsing in a dose-dependent manner by inducing persistent cytosolic translocation. In contrast, the other five growth factors increased the fraction of pulsing cells above the baseline. Exposure of cells to BTC, HGF, or HRG resulted in a progressive increase in the fraction of pulsing cells over a  $\sim 40$ -fold concentration range (Figure 4B; blue, green, and yellow lines), whereas exposure to EGF or EPR resulted in a sudden increase in pulsing over a narrow  $\sim 2$ -fold range in ligand concentration (cyan and pink). Similar data were obtained in F3aN400-Venus expressing MCF10A cells, a second normal mammary epithelial cell line, except that these cells were less sensitive to BTC and more sensitive to EGF than 184A1 cells (Figure S4B). We conclude that differences in identities and concentrations of an extracellular ligand result in consistent differences in FOXO3 translocation dynamics, as expected for dynamical encoding.

To determine whether the trend and pulsatile components of FOXO3 translocation dynamics carry different information (Hansen and O’Shea, 2015), we calculated the mutual information between fPCA scores for the synchronous response between  $t = -70$  to  $80$  min and the discretized pulse scores between  $80$  and  $1,580$  min. Variation in early fPCA scores typically explained  $<20\%$  of the variation in the late pulsatile response and was ligand dependent (Figures 4C and S3C). In this context, this represents a low level of mutual information since trajectories from IGF1-treated cells, in which pulsing is low, exhibited over 60% mutual information between early and late phases (Figure S3C).

### Figure 3. Early Synchronous Response of F3aN400-Venus Translocation Varies with Growth Factor Identity

- (A) Schematic of fPCA performed on F3aN400-Venus trajectories between  $t = -70$  and  $80$  min. Three example trajectories are shown on the left; fPC1, fPC2, and fPC3 harmonics in the middle; and score plots on the right. fPC1 corresponds to a pre-treatment baseline harmonic, fPC2, a post-treatment sustained harmonic and fPC3, a post-treatment transient harmonic. fPC1–3 explain 58%, 35%, and 3% of observed variance across all ligands (respectively).
- (B) Plot of fPC2 versus fPC3 scores for six growth factors at 100 ng/mL. Large oval regions represent 95% confidence intervals for scores computed for all trajectories on a per-growth factor basis.
- (C) Pairwise comparison of fPCA scores by growth factor; significant differences are highlighted in gray ( $p$  value  $< 10^{-10}$ ; Wilcoxon rank-sum test).
- (D) Median values of fPCA scores from different growth factors at various concentrations, fitted with linear models (solid lines). Datapoints with significantly different scores from untreated controls are depicted as solid points while those with  $p$  value  $> 10^{-10}$  are depicted as unfilled points. See also Figure S2B.
- (E) Heat maps of 40 selected F3aN400 trajectories (with high pulse scores) in 184A1 cells treated with 100 ng/mL EGF. Left panel shows “trend” response generated by combining the first five harmonics from fPCA analysis on a per-trajectory basis. Right panel subtracts the computed trend from experimental trajectories revealing pulsing. Red and blue arrowheads denote  $t = 0$  and  $t = 80$  min (see Figure 1D for comparison).
- (F) Spectral density analysis of detrended F3aN400 trajectories ranked by pulse score (gray lines; see Figure 4 for method used to calculate pulsing). The spectrum for a simple sinusoid with sampling noise similar to that of experimental data is shown in light blue line and simulated pink noise in pink line are shown for comparison.

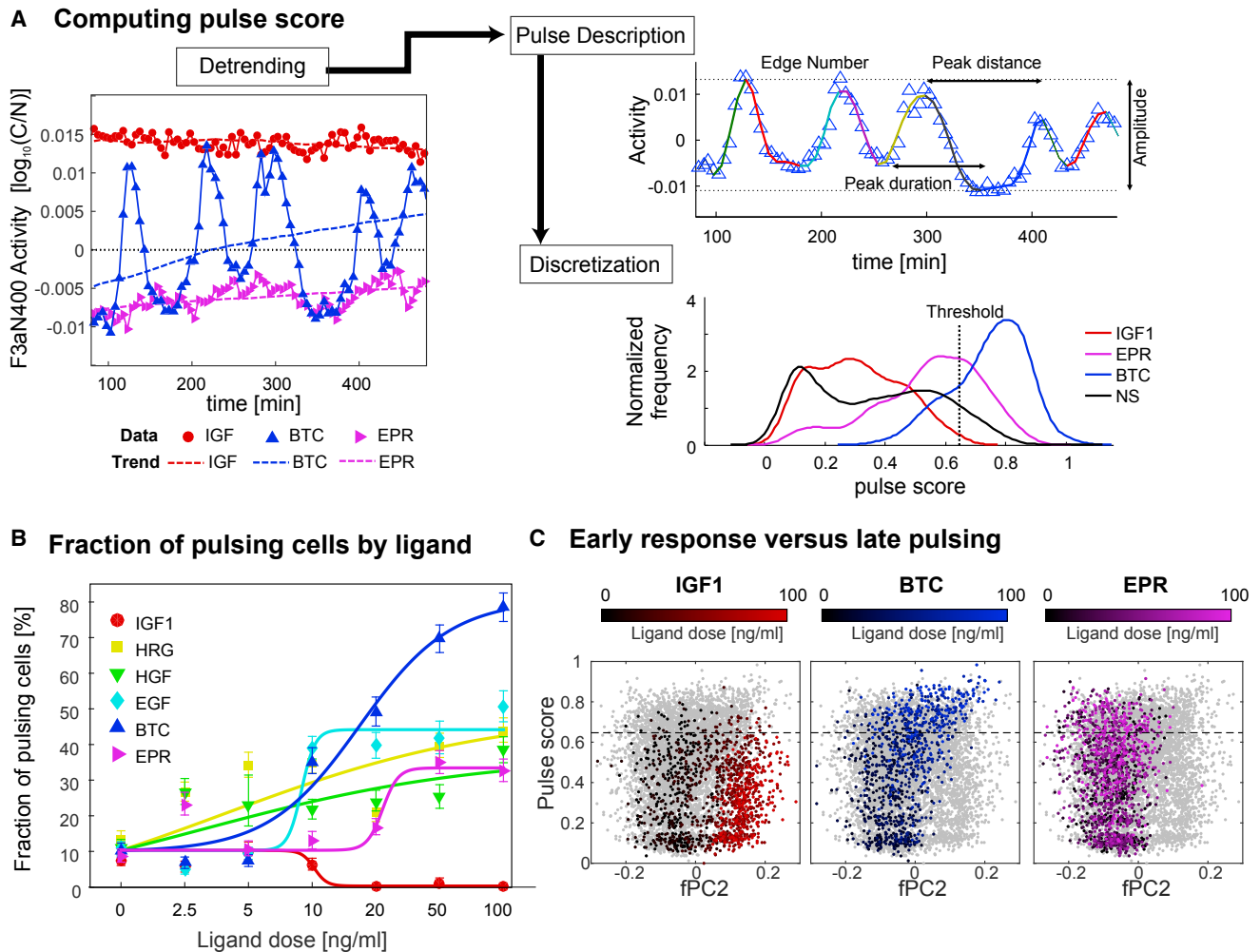


**Figure 4. Late Pulsing of F3aN400 Translocation also Exhibits Ligand-Dependent Dynamics**

(A) Schematic of method used to compute pulse scores. Left: F3aN400-Venus trajectories for three ligands (each at 100 ng/mL) detrending between  $t = 80$  and 1,580 min by fPCA on a per-trajectory basis (dotted lines represents the computed trends). Upper right: Computing pulse score using a peak detection algorithm and pulse score calculated from a nonlinear combination of the (1) number of edges, (2) pulse amplitude, (3) signal-to-noise ratio (not shown), (4) peak duration, and (5) peak distance. See details in [STAR Methods](#). Lower right: Discretization of pulse scores; dotted line depicts a threshold at  $\sim 0.6$ .

(B) Fraction of cells with pulsing F3aN400-Venus reporter based on ligand dose and identity, as scored by the algorithm described in (A). Solid lines show fitted trends based on Hill's equation. Error bars represent bootstrap confidence intervals computed from single-cell pulse scores at each ligand dosing (bootstrapping was performed using the MATLAB function, `bootci` with  $\alpha = 0.32$ ).

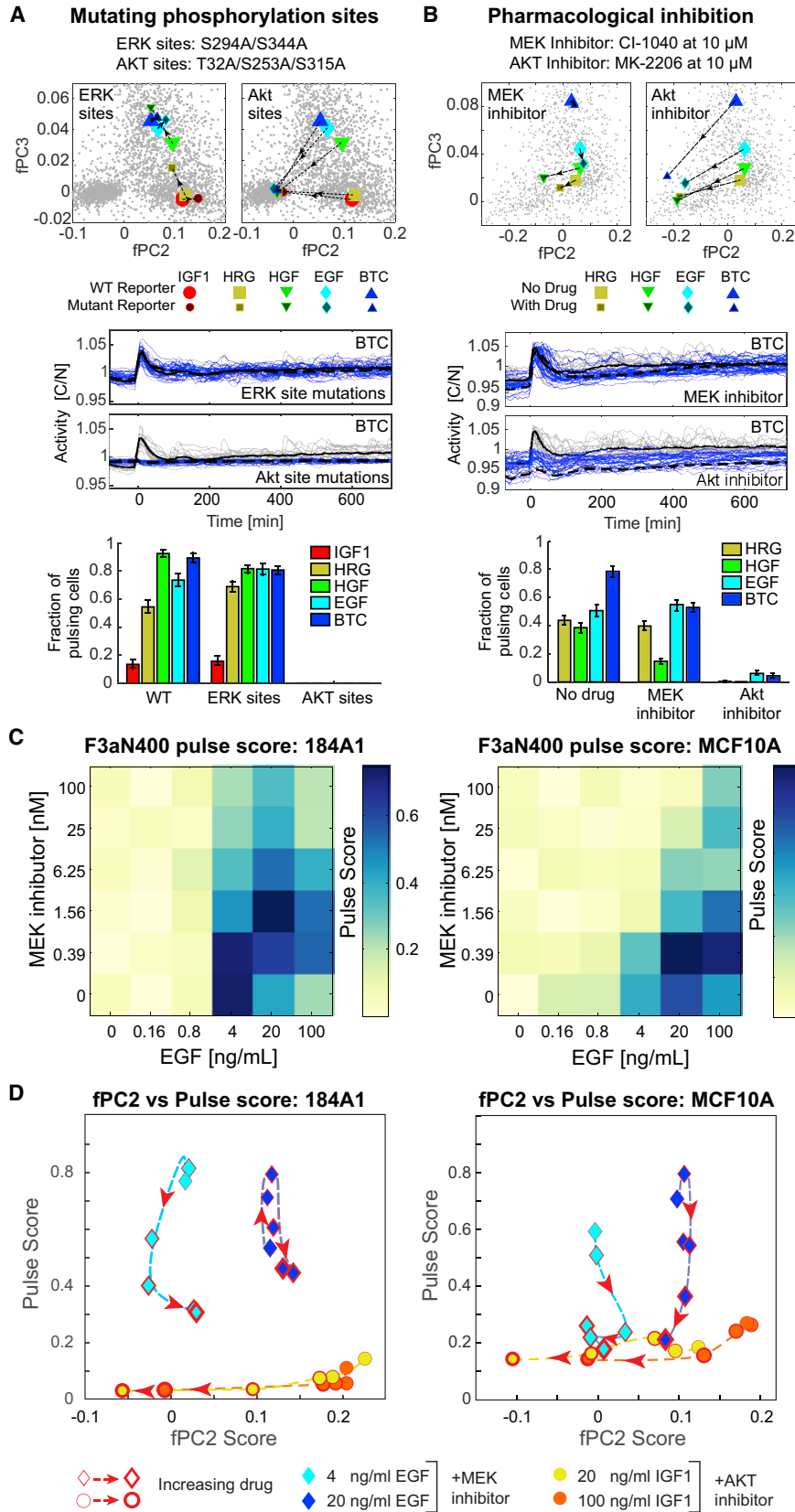
(C) Comparison of fPC2 versus pulse score for trajectories collected from cells exposed to IGF1, BTC, and EPR. Shading represents ligand concentration, ranging from lowest (0 ng/mL, black dots) to highest (100 ng/mL, colored dots). Light gray data points represent all other conditions. Dotted lines depict the pulse score threshold for discretization.

These data suggest that early and late FOXO3 translocation dynamics are largely independent of each other and therefore have the potential to encode different information (except in the case of IGF1 in which little pulsing is observed).

### Regulation of FOXO3 Dynamics by Akt and ERK

Information is transduced from transmembrane receptors to FOXO3 via cytosolic kinase cascades, among which those involving Akt and ERK are best understood. Previous work from our group has shown that growth factors differentially activate ERK and Akt signaling in mammary cells (Niepel et al., 2014) and blotting for FOXO3 phosphorylation on S253 and S294

confirmed that differences in kinase activity are transmitted to the F3aN400-Venus sensor (Figure 1C). To investigate the functions of post-translational modification, we engineered serine/threonine to alanine mutations into the F3aN400-Venus sensor at known phosphorylation sites (Figure S4A). Translocation dynamics were quantified by fPCA in the early phases (from  $-70$  to 80 min) and pulse score in the late phase (from 80 to 1,580 min). In 184A1 cells, a triple point mutation in Akt sites (T32A/S253A/S315A) totally inhibited cytosolic translocation under all conditions, reducing fPC2 and fPC3 scores to near zero and also eliminating pulsing (Figure 5A). In contrast, mutation of ERK-specific sites (S294A/S344A) had a relatively small effect



(legend on next page)

on either fPCA scores or pulsing, and differences among ligands were retained (Figure 5A). Akt inhibition with MK-2206 phenocopied T32A/S253A/S315A mutation by eliminating all cytosolic translocation and pulsing (Figure 5B). Similar data were obtained in F3aN400-Venus expressing MCF10A cells (Figure S4B).

To further investigate the role of MEK/ERK signaling in pulsing, 184A1 and MCF10a cells were exposed to PD0325901 and EGF in combination over a range of concentrations and pulse score was measured (Figure 5C). In both cell types, low-dose MEK inhibitor increased pulse scores above the level observed with EGF alone (to a maximum of 0.8), but as drug concentration increased above 2 nM, pulse score then fell monotonically to a minimum of ~0.3. Because CI-1040 and PD0325901 are among the most selective kinase inhibitors known (they are non-ATP-competitive), off-target effects are unlikely. We conclude that MEK and ERK are likely to regulate F3aN400-Venus pulsing indirectly or via unmapped modification sites.

To examine the interplay between pulsing and early synchronous translocation, cells were exposed to growth factors in combination with inhibitors of Akt or MEK inhibitors over a range of concentrations. Dynamics were then analyzed on a landscape of early fPC2 score versus pulse score. In 184A1 cells treated with IGF1, fPC2 score varied with ligand dose, pulse score was low, and addition of Akt inhibitor resulted in a dose-dependent shift along the fPC2 axis, showing that IGF1 primarily regulates FOXO3 via Akt (Figure 5D, orange and yellow data points). Exposure of cells to different levels of EGF changed both fPC2 and pulse scores (Figure S5A; this was true of other ligands as well; Figure S5B). Complete inhibition of the Akt pathway reduced fPC2 and pulse score to zero (Figure S5A; black square dot). The effects of MEK inhibition were more complex: in 184A1 cells exposed to 20 ng/mL EGF, MEK inhibitor increased pulsing 2-fold at intermediate drug concentrations and then reduced it at higher concentrations. At lower EGF concentrations, progressively higher doses of MEK inhibitor resulted in a monotonic decrease in pulsing. Taken together, these data suggest that (1) complete inhibition of Akt blocks cytosolic translocation of F3aN400-Venus under all conditions, (2) partial inhibition of Akt suppresses both the trend and pulsing responses, (3) pulsing is also regulated by MEK/ERK signaling, although not via known sites of FOXO3 modification, and (4) at high ligand levels, fractional inhibition of MEK/ERK can increase pulsing, implying that signaling is saturated.

### FOXO3 Integrates ERK and Akt Dynamics

To study the relationship between ERK and FOXO3 dynamics in single cells, we constructed a dual reporter in which F3aN400-

mCherry was linked to EKAREV, a FRET-based reporter of ERK kinase activity (Albeck et al., 2013; Aoki et al., 2013), via a type 2A self-cleaving peptide (Figure 6A). Trajectories were normalized using trend lines derived from fPCA or spline-fitting and scaled individually by the max-min range for that reporter (to correct for differences in reporter-intrinsic intensity and dynamic range). In MCF10A cells, we found that ERK activity and nuclear-to-cytosolic translocation of F3aN400-mCherry cells tracked each other before and after stimulation with BTC (typical pairs of F3aN400 and EKAREV activity trajectories are shown in the upper left panel of Figure 6B; more examples are shown in Figure S6). Across a set of ~30 F3aN400 and EKAREV trajectories, a median Pearson's correlation coefficient of  $R \sim 0.83$  was obtained for the two trajectories using a sliding 90-min window (Figure 6B, upper right panel). When cells were stimulated with BTC for 4 hr and then treated with the Akt inhibitor (1  $\mu$ M of MK2206), F3aN400-mCherry stopped pulsing, but EKAREV dynamics were not appreciably altered, causing the two trajectories to decorrelate (median  $R = -0.03$ ; Figure 6B, middle panels). When BTC-stimulated cells were treated with MEK inhibitor (1  $\mu$ M of CI1040) at  $t = 4$  hr, pulsing by both EKAREV and F3aN400-mCherry was largely eliminated and trajectories became decorrelated (median  $R = 0.17$ ; Figure 6B, bottom panels). We conclude that the EKAREV and F3aN400-mCherry undergo synchronous pulsing in a manner that requires both Akt and ERK activity. When growth factors were compared, EKAREV and F3aN400-mCherry were most highly correlated when pulse scores were high (e.g., with BTC, EPR, and EGF as ligands;  $p < 0.01$  using Wilcoxon rank-sum test against unstimulated cells) and least correlated when pulse scores were low (e.g., with IGF1; Figures 6C and 6D). Thus, FOXO3 pulsing appears to originate from the dynamics of ERK activity while also requiring activation of the Akt pathway.

### Exploring the Connectivity of ERK, Akt, and FOXO3 in Breast Cancer Cell Lines

To determine how FOXO3 translocation varies across cell lines, we selected, from a panel of widely studied breast cancer cells, seven lines that include HER2<sup>AMP</sup>, hormone-receptor positive, and triple negative subtypes (the ICBP43 set [Li et al., 2013]); 184A1 and MCF10A cells were included as examples of normal mammary epithelial controls. Mutations in mitogenic signaling networks are common in breast cancer, and multiple cell lines in our collection carry oncogenic mutations in *HRAS*, *KRAS*, *BRAF*, and *PIK3CA*. To study FOXO3 localization in these cells we used fixed-cell immunofluorescence at seven time points 15 to 240 min following exposure of cells to one of seven growth factors at 100 ng/mL. The average level of FOXO3 activation was

#### Figure 5. ERK/Akt Combinatorial Regulation on FOXO3 Dynamical Encoding

(A and B) Effects on F3aN400-Venus dynamics in 184A1 cells with (A) mutations in phosphorylation sites or (B) MEK and AKT inhibitors. Top panels: early response in an fPC2-vs-fPC3 landscape for multiple ligands; arrows depict change from wild-type to mutant reporter (or with and without drug). Middle panels: trajectories for reporters without (gray) or with (blue) phospho-site mutants or drugs in BTC-treated cells. Lower panels: pulse scores for multiple ligands (error bars represent standard errors from bootstrapping). See Figure S4B for MCF10A data.

(C) Averaged pulse scores (for >100 trajectories per condition) in F3aN400-Venus expressing 184A1 and MCF10A cell lines pre-treated with the MEK inhibitor PD0325901 at 0–100 nM for 1 hr and subsequently exposed to EGF at 0–100 ng/mL.

(D) Plot of fPC2 versus pulse score for 184A1 or MCF10a cells pre-treated with the MEK inhibitor PD0325901 at five doses (0.39, 1.56, 6.25, 25, 100 nM) or Akt inhibitor MK-2206 at four doses (6.25, 25, 100, 500 nM) and then with EGF at 4 ng/mL (cyan diamond) or 20 ng/mL (blue diamond) or IGF1 at 20 ng/mL (yellow circles) or 100 ng/mL (orange circles), respectively. Directional arrows and the thickness of the outlines denote increasing drug concentration.

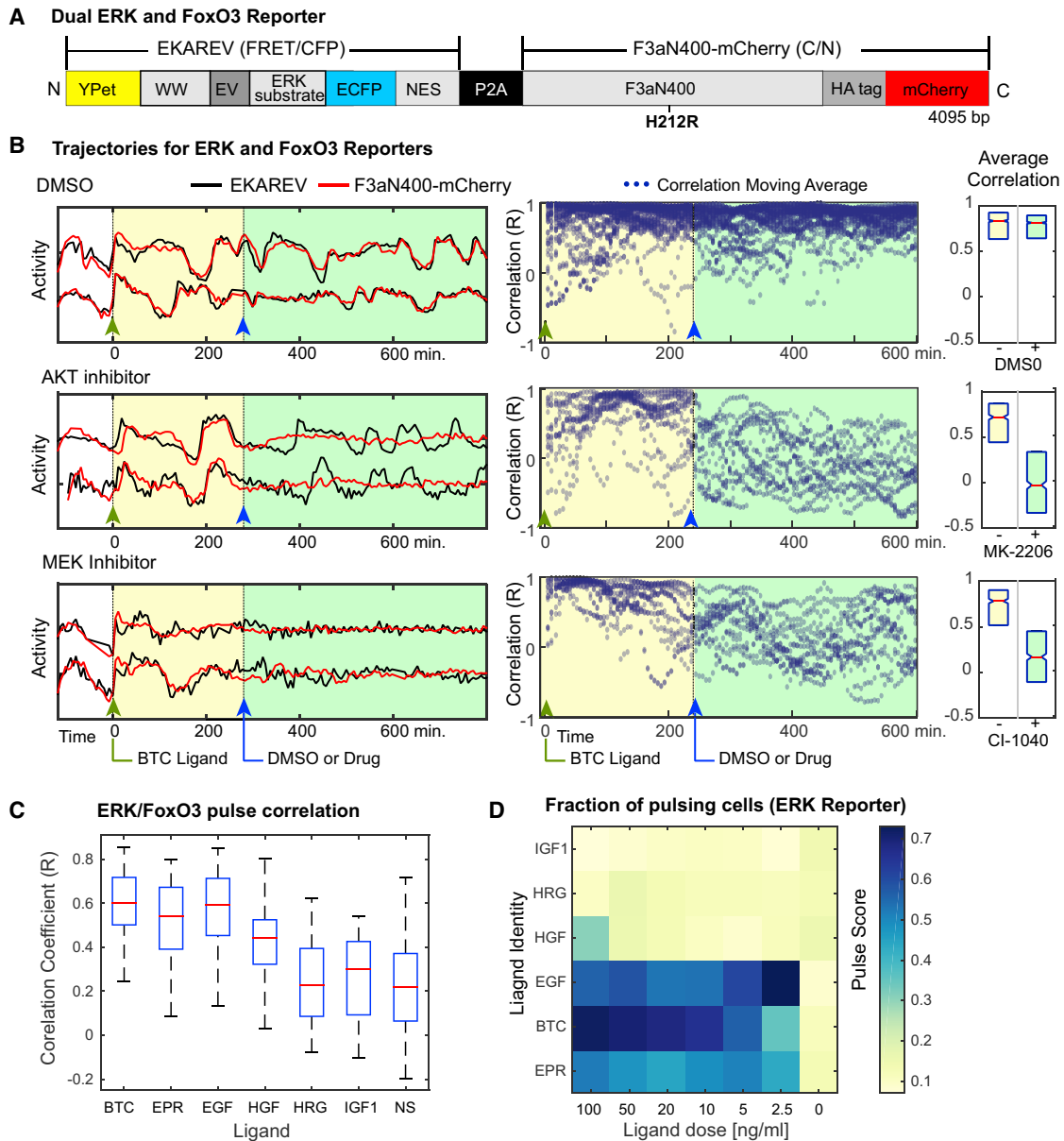


**Figure 6. In-Phase Pulsing of ERK Activity and FOXO3 Translocation**

(A) Schematic of a dual reporter for ERK (EKAREV) and FOXO3 (F3aN400) linked via a P2A self-cleaving peptide. EKAREV activity was quantified from the FRET/CFP signal ratio and F3aN400-mCherry by C/N ratio.

(B) Detrended trajectories (scaled by max-min range to facilitate comparison) for EKAREV (black) and F3aN400-mCherry (red) in serum-starved MCF10A cells expressing the dual reporter construct. Cells were exposed at  $t = 0$  hr (denoted by green arrowhead) to 100 ng/mL BTC followed at  $t = 4$  hr (blue arrowhead) by DMSO, Akt inhibitor ( $1 \mu\text{M}$  MK-2206), or MEK inhibitor ( $1 \mu\text{M}$  CI-1040). Correlation coefficients (middle panels) were calculated using a  $\sim 90$ -min sliding window, and median scores are shown as box blots (right panels) for all trajectories prior to (yellow) and after drug exposure (green). Boxplots depict the 25th, 50th (in red) and 75th percentiles of the correlation coefficients.

(C) Correlation coefficients for EKAREV activity and F3aN400 translocation pulsing in cells exposed to different growth factors at 100 ng/mL. Boxplots depict the first, second (in red), and third quartiles of the correlation coefficient. The whiskers span from  $Q1 - 1.5 \times \text{IQR}$  to  $Q3 + 1.5 \times \text{IQR}$  where  $Q1$  is the first quartile,  $Q3$  is the third quartile, and IQR is the interquartile range (this span represents 99.3% of all values).

(D) Fraction of pulsing cells based on the EKAREV reporter following stimulation with different growth factors and doses.

captured by the median value of the FOXO3 C/N ratio; the median IQR of the C/N ratio served as a proxy for pulsing compatible with fixed-cell imaging (as described above; Figure 7A). Across all ligands and time points, normal mammary 184A1

and MCF10A exhibited the widest range of signaling states, whereas breast cancer cells exhibited narrower ranges (Figure 7B). BT20 and T47D cell lines, which carry activating mutations in the catalytic p85 subunit of PI3K (*PIK3CA*), were confined

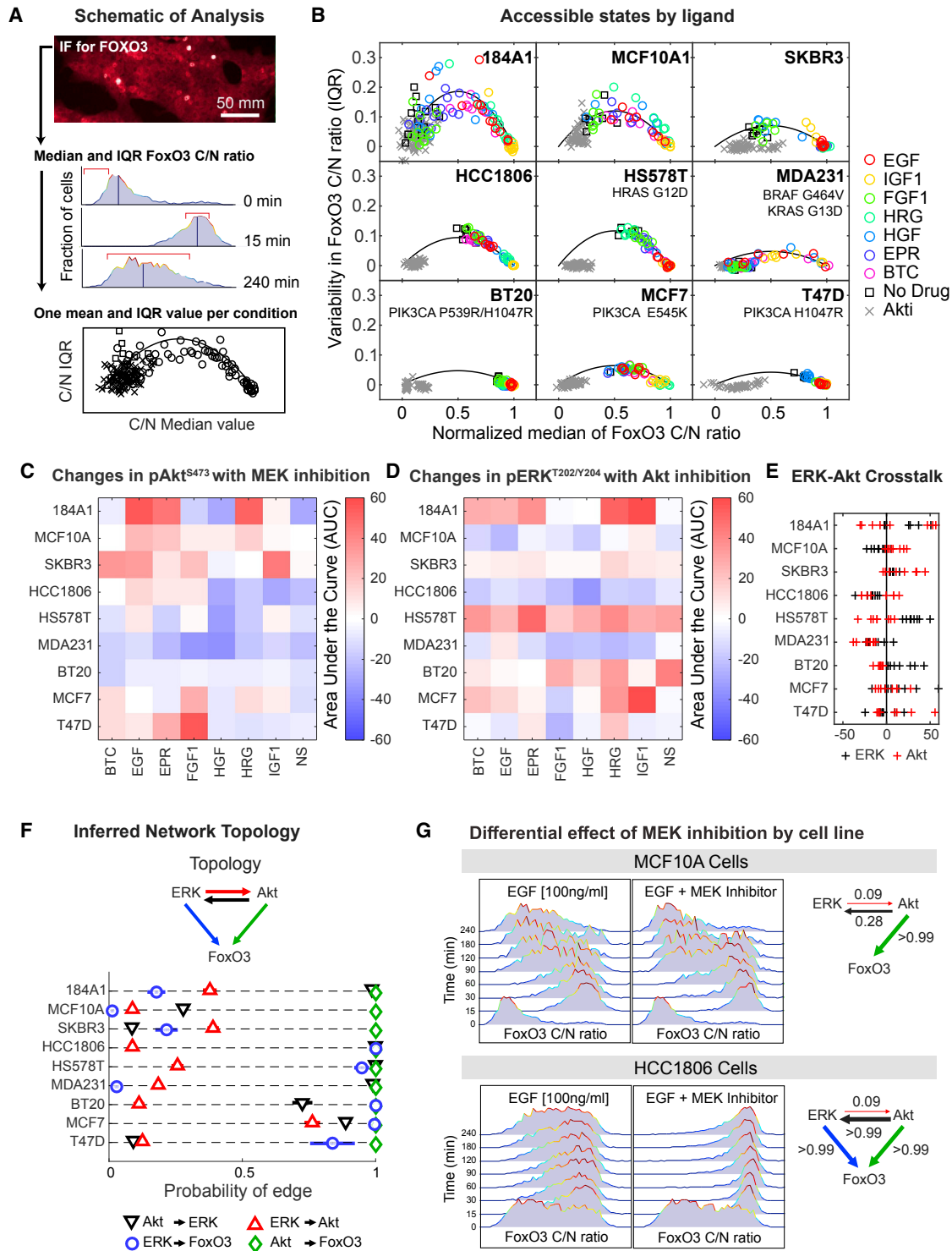


**Figure 7. Diversity of Interactions among ERK, Akt, and FOXO3 in Breast Cancer Cell Lines**

(A) Schematic of FOXO3 analysis in cancer cell lines by immunofluorescence imaging. Median C/N ratio captures overall activity and interquartile range (IQR) the extent of cell-to-cell variability, which arises in part from pulsing. Values were obtained from >1,000 fixed cells per condition; see [STAR Methods](#) for details on normalization methods.

(B) Relationship between median values and IQR of FOXO3 C/N ratios across breast cancer cell lines. Cells were serum-starved and pre-treated with DMSO or 10  $\mu$ M MK2206 for 1 hr and then exposed to growth factors at 100 ng/mL followed by immunostaining with anti-pERK<sup>T202/Y204</sup>, anti-pAkt<sup>S473</sup>, or anti-FOXO3 antibodies. Each datapoint corresponds to one post-treatment time point.

(legend continued on next page)

to the fully active state (high C/N ratio) even in the absence of ligand, whereas BRAF<sup>G464V</sup>/KRAS<sup>G13D</sup> MDA231 cells exhibited intermediate median C/N ratios and low IQR, suggesting reduced pulsing (Figure 7B). We infer that activating mutations in either the Akt or ERK pathways reduce the accessible dynamic range over which FOXO3 can respond to growth factors.

Based on current understanding of immediate-early signaling, ERK could either regulate FOXO3 directly by phosphorylating it on S294, S344, or S425 (Yang et al., 2008) or it could act indirectly via negative cross-talk on Akt (Moelling et al., 2002; Yu et al., 2002). To begin to distinguish between these possibilities, we measured cross-regulation between ERK and Akt in different cell lines exposed to one of seven growth factors. The effect of MEK/ERK on AKT was assessed by measuring pAkt<sup>S473</sup> levels in the presence and absence of MEK inhibition and the effect of AKT on MEK/ERK by pERK<sup>T202/pY204</sup> levels was measured in the presence and absence of Akt inhibition (Figures 7C–7E). This experiment revealed a wide range of possible interactions between Akt and ERK depending on ligand and cell type. For example, inhibition of Akt with MK2206 following IGF1 exposure significantly increased pERK<sup>T202/pY204</sup> levels in 184A1 cells but had little effect in MCF10A cells (Figure 7D).

We then used dynamic Bayesian network analysis (Friedman et al., 2000; Hill et al., 2012) to infer the connectivity of ERK, Akt, and FOXO3 as assessed by either the median or IQR of the C/N ratio under 32 different conditions (4 inhibitor conditions × 8 ligand conditions) for each cell line (Figure S7A). We found that the probability of edges corresponding to Akt → FOXO3, ERK → FOXO3, and Akt ↔ ERK varied to a significant degree with cell line and ligand (Figure 7F). Probability values also varied with the learning method, as expected for probabilistic analysis of noisy data, but overall agreement was quite good: BGe and BDe scoring algorithms exhibited 94% and 81% agreement with dynamic Bayesian network (DBN) results (Figures S7B–S7D), suggesting that inferred edge probabilities are likely to be reliable in aggregate (Heckerman et al., 1995). In all cell lines, we found strong evidence of an Akt → FOXO3 interaction, and in HCC1806, HS578T, BT20, and T47D, the probability of an ERK → FOXO3 interaction was high. Akt ↔ ERK interactions were strongest in MCF7 cells (Figure 7F). Comparison of FOXO3 translocation in MCF10a and HCC1806 cells exemplified this difference. ERK → FOXO3 interaction was inferred to be substantially stronger in HCC1806 than MCF10 cells and MEK inhibition had a substantially greater effect on the distribution of FOXO3 C/N values in HCC1806 than MCF10A cells (Figure 7G). We conclude that networks regulating FOXO3 differ in topology from one cell type to the next and that ERK can probably control pulsing via both Akt-dependent and Akt-independent mechanisms.

## DISCUSSION

In this article, we analyze the temporal regulation of FOXO3, a mammalian transcription factor controlled in a combinatorial manner by multiple signal transduction pathways. We focused on nuclear-cytosolic translocation induced by growth factors and its regulation by the ERK and Akt kinase cascades. Relocalization plays an important role in the regulation of transcription factors and has recently been shown by live-cell imaging to involve pulses of active and inactive states. In the case of mammalian transcription factors, such as NF-κB and TP53 (Batchelor et al., 2008; Tay et al., 2010) and yeast Msn2 and Crz1 (Cai et al., 2008; Hao and O’Shea, 2011), modulation of the timing and duration of nuclear-cytosolic translocation carries information about the strength and identity of the initiating stimulus (Hansen and O’Shea, 2016; Tay et al., 2010). We build on these concepts by demonstrating that FOXO3 dynamics comprise early and late phases that respond independently to differences in the relative activities of ERK and Akt kinases, which are determined in turn by growth factor identity and concentration (all data are available for reanalysis in an NIH LINCS format at <http://lincs.hms.harvard.edu/sampattavanich-cellsyst-2018/>). The early FOXO3 response to ligand is synchronous across all cells and relatively short-lived; the late phase is pulsatile and can last for 24 hr or more. The synchronous response is strongest for ligands such as IGF1 and weakest for EPR and BTC; the opposite is true of the pulsatile response. These features of FOXO3 appear to be reflective of the interplay between ERK and Akt signaling and provide FOXO3 with significant information-encoding capacity. Although we have not yet linked differences in FOXO3 dynamics to differential transcriptional activity, we speculate that the diversity of dynamical responses is relevant to the diverse biological activities of FoxO class of transcription factors.

### Ligand Identity Is Transmitted by Relative Akt and ERK Activities and Encoded in FOXO3 Dynamics

Across a wide range of ligand types and concentrations, FOXO3 translocation dynamics have two distinct temporal phases. Within 15 to 20 min of growth factor addition, FOXO3 moves from the nucleus to the cytoplasm in near-synchrony across all ligand-activated cells in the population. FOXO3 then shuttles back and forth between the two compartments for up to 24 hr. Early synchronous translocation of FOXO3 appears to be regulated primarily by the intensity of Akt activity. Subsequent pulsing is asynchronous and occurs in phase with pulses of ERK activity; when Akt is active, pulses of ERK activity correspond to periods of FOXO3 cytosolic localization. For many ligands, mutual information between early and late dynamics is

(C and D) Heatmap showing effect of MEK inhibition (CI1040, 10 μM) on the area under the curve of pAkt<sup>S473</sup> levels or of Akt inhibition (MK2206, 10 μM) on the area under the curve of pERK<sup>T202/Y204</sup> levels 0–240 min for each cell line/ligand combination.

(E) Cross-talk between the ERK and Akt pathways. Changes in pERK<sup>T202/Y204</sup> levels caused by Akt inhibitor (black data points) or changes in pAkt<sup>S473</sup> levels caused by MEK inhibitor (red data points) for each ligand and cell line combination.

(F) Dynamic Bayesian network (DBN) modeling of data described in (B) and (E) to infer the probability of Akt → FOXO3, ERK → FOXO3, and Akt ↔ ERK edges. The resulted edge probabilities are shown in the bottom panel with error bars indicating the standard deviation of predictions across multiple independent runs with noise added to the data. See also Figure S7 for similar analyses using BGe and BDe scoring methods.

(G) Comparison of FOXO3 translocation dynamics between HCC1806 and MCF10A cells exposed to 100 ng/mL EGF with and without MEK inhibitor. Diagrams on the right show corresponding probabilities from DBN analysis for each edge interaction as calculated in (F).

low (<20%), suggesting that the two temporal phases can carry distinct information.

Different growth factors induce Akt and ERK to different degrees (Niepel et al., 2014), and this correlates well with the degree of phosphorylation of FOXO3 on Akt and ERK-dependent sites and the extent to which a ligand provokes the two phases of FOXO3 dynamics. For example, IGF1 signals strongly through Akt and primarily induces a harmonic in the principal component decomposition of FOXO3 trajectories that remains high for an extended period of time, whereas BTC signaling is biased toward ERK rather than Akt and primarily induces a harmonic that peaks at  $t = 15$  min and then falls back to baseline. Because individual target genes can respond preferentially to constant or oscillatory patterns of transcription factor activity (Purvis et al., 2012; Tay et al., 2010), we speculate that FOXO3 dynamics are readout at the level of target genes involved in cell death, cell cycle progression, reactive oxygen species detoxification, etc. (Jensen et al., 2011; Purvis et al., 2012; Tay et al., 2010). However, our data do not address how this might be achieved; in well-characterized systems such as *TP53*, kinetically related genes do not fall neatly into clusters of similar function (Porter et al., 2016).

Pulsatile regulation of transcription factors is often described as oscillatory, but in the case of FOXO3, spectral density analysis does not reveal a dominant frequency, a key characteristic of a conventional oscillator. Thus FOXO3 does not exhibit either AM or FM encoding (Levine et al., 2013). Instead, we observe a  $1/f$  spectrum (where  $f$  is frequency), a common characteristic of multiscale dynamical systems. In F3aN400-Venus trajectories, the  $1/f$  power spectrum (also known as pink noise) is convolved by a relatively weak but statistically significant periodic signal with a wavelength of  $80 \pm 30$  min ( $\sim 0.2$  mHz), considerably faster than the oscillations of *TP53* (which have a periodicity of 3–5 hr) (Purvis et al., 2012), but similar to NF- $\kappa$ B (periodicity  $\sim 1.5$  hr) (Kellogg and Tay, 2015). The origins of  $1/f$  and periodic components of FOXO3 trajectories remain unknown.

### Combinatorial Control over FOXO3 Activity

The relationship between FOXO3 pulsing and Akt or ERK activity is complex and non-monotonic. For example, in two cell lines we studied in detail, the highest pulse scores for EGF are observed when ligand concentrations are sub-saturating or ERK is partially inhibited. This effect may be indirect, as the Akt and ERK kinase cascades are known to have multiple mechanisms of cross-regulation, involving both ERK-dependent inhibition of Akt (Yu et al., 2002) and PI3K/Akt-dependent inhibition or stimulation of ERK (Moelling et al., 2002). Our data suggest that ERK regulation of FOXO3 kinetics is at least partly indirect, perhaps via modulation of Akt activity. However, the strength of such cross-talk (as measured by the effect of Akt inhibition on ERK activity and vice-versa) varies with cell line and with ligand. Moreover, whereas our experiments artificially vary FOXO3 dynamics over a range of states using ligands and ERK and Akt inhibitors in combination, we speculate that this is achieved physiologically by the combined activities of multiple activating and inhibitory signal transduction cascades.

In tumor cells carrying mutations in ERK and Akt signaling proteins, such as the p85 subunit of PI3K (PIK3CA), HRAS, PTEN

phosphatase, etc., the range of dynamical states that can be accessed for FOXO3 in response to growth factors is lower (often much lower) than in normal epithelial cells. In some cell types (BT20 for example), FOXO3 is chronically localized in the cytosol and growth factors have little or no effect. In HCC1806 or SKBR3 cells, multiple ligands can promote cytosolic translocation, but the range of dynamical states is less than in normal epithelial cells. This suggests that FOXO3 trajectories encode less information in cancer than normal cells. However, more complete understanding of the effects of oncogenic mutations on FOXO3 will require dynamical data from both transformed and non-transformed cell types rather than the fixed-cell imaging used to compare tumor cells in the current study.

### Conclusion

In the past few years, it has been shown that multiple transcription factors and signal transduction kinases alternate between active and inactive states on time scales of minutes to hours. It has been suggested that such systems can encode information via variation in amplitude (AM encoding) or frequency (FM encoding). FOXO3 dynamics do not conform to either of these possibilities but instead involve independently regulated early and late phases. Late-phase pulsing by FOXO3 is non-oscillatory and synchronous with ERK pulsing, which has been proposed to originate from the stochastic release of autocrine factors among adjacent cells (Sparta et al., 2015). Alternatively, FOXO3 might be regulated by an excitable intracellular feedback circuit subject to stochastic fluctuation (although a pure oscillator degraded by Poisson noise is not expected to have a  $1/f$  power spectrum) or a chaotic feedback oscillator (Novak and Tyson, 2008). Regardless, multi-part dynamical trajectories represent a potential mechanism for combinatorial control over transcription. It will be interesting to determine whether other transcription factors, including other members of the FoxO family, also have multi-part dynamical trajectories controlled by ligand identity.

### STAR★METHODS

Detailed methods are provided in the online version of this paper and include the following:

- **KEY RESOURCES TABLE**
- **CONTACT FOR REAGENT AND RESOURCE SHARING**
- **EXPERIMENTAL MODEL AND SUBJECT DETAILS**
  - Tissue Culture Cell Lines
- **METHOD DETAILS**
  - Tissue Culture
  - Construction of Plasmids and Reporter Cell Line Establishment
  - Analysis of Total Cellular Lysates
  - Fixed and Live-Cell Microscopy
- **QUANTIFICATION AND STATISTICAL ANALYSIS**
  - Calculation of FoxO3 Translocation Activity
  - Scaling of Western Blots; Error Propagation; Total Least Squares
  - Functional Principal Component Analysis (fPCA)
  - Pulse Score and Fraction of Pulsing Cells
  - Power Spectrum Analysis

- Mutual Information
- Fixed-Cell Analysis of ERK-AKT-FoxO3 Connectivity
- Quantifying ERK, AKT and FoxO3 Response to Inhibitors
- Approach to Bayesian Model Comparison
- Comparing Model Topologies
- Computing Dynamic Bayesian Networks
- DBN Learning with the BGe Score
- DBN Learning with g-prior Based Gaussian Score
- DBN Learning with the BDe Score
- DATA AND SOFTWARE AVAILABILITY

## SUPPLEMENTAL INFORMATION

Supplemental Information includes nine figures, one table, and one video and can be found with this article online at <https://doi.org/10.1016/j.cels.2018.05.004>.

## ACKNOWLEDGMENTS

This work was funded by 50GM107618 and U54HL127365 to PKS, a “Chalermphrakiat” Grant (Mahidol University) and the Thai Research Fund (TRG5880094) to SS, and the German BMBF (SBEpo 0316182A and 0316042G) to BS. We thank J. Timmer, V. Becker, J. Sims, J. Waters, H. Elliott, the HMS-Nikon and IDAC Core Facilities, K. Aoki for EKAREV plasmid, and A. Bradley for PiggyBAC.

## AUTHOR CONTRIBUTIONS

Conceptualization, S.S., P.K.S.; Methodology, S.S., P.K.S., J.G.A.; Investigation, S.S., B.A.K.; Formal Analysis, S.S., B.S., B.M.G.; Writing P.K.S., S.S., B.S., B.M.G., J.G.A.; Funding Acquisition, P.K.S.

## DECLARATION OF INTERESTS

None.

Received: August 3, 2016

Revised: December 19, 2017

Accepted: May 4, 2018

Published: June 6, 2018

## REFERENCES

- Albeck, J.G., Mills, G.B., and Brugge, J.S. (2013). Frequency-modulated pulses of ERK activity transmit quantitative proliferation signals. *Mol. Cell* 49, 249–261.
- Aoki, K., Kumagai, Y., Sakurai, A., Komatsu, N., Fujita, Y., Shionyu, C., and Matsuda, M. (2013). Stochastic ERK activation induced by noise and cell-to-cell propagation regulates cell density-dependent proliferation. *Mol. Cell* 52, 529–540.
- Bak, P., Tang, C., and Wiesenfeld, K. (1987). Self-organized criticality: an explanation of the 1/f noise. *Phys. Rev. Lett.* 59, 381–384.
- Batchelor, E., Loewer, A., Mock, C., and Lahav, G. (2011). Stimulus-dependent dynamics of p53 in single cells. *Mol. Syst. Biol.* 7, 488.
- Batchelor, E., Mock, C.S., Bhan, I., Loewer, A., and Lahav, G. (2008). Recurrent initiation: a mechanism for triggering p53 pulses in response to DNA damage. *Mol. Cell* 30, 277–289.
- Biggs, W.H., 3rd, Meisenhelder, J., Hunter, T., Cavenee, W.K., and Arden, K.C. (1999). Protein kinase B/Akt-mediated phosphorylation promotes nuclear exclusion of the winged helix transcription factor FKHR1. *Proc. Natl. Acad. Sci. USA* 96, 7421–7426.
- Brunet, A., Bonni, A., Zigmond, M.J., Lin, M.Z., Juo, P., Hu, L.S., Anderson, M.J., Arden, K.C., Blenis, J., and Greenberg, M.E. (1999). Akt promotes cell survival by phosphorylating and inhibiting a Forkhead transcription factor. *Cell* 96, 857–868.
- Brunet, A., Kanai, F., Stehn, J., Xu, J., Sarbassova, D., Frangioni, J.V., Dalal, S.N., DeCaprio, J.A., Greenberg, M.E., and Yaffe, M.B. (2002). 14-3-3 transits to the nucleus and participates in dynamic nucleocytoplasmic transport. *J. Cell Biol.* 156, 817–828.
- Brunet, A., Park, J., Tran, H., Hu, L.S., Hemmings, B.A., and Greenberg, M.E. (2001). Protein kinase SGK mediates survival signals by phosphorylating the forkhead transcription factor FKHRL1 (FOXO3a). *Mol. Cell Biol.* 21, 952–965.
- Cai, L., Dalal, C.K., and Elowitz, M.B. (2008). Frequency-modulated nuclear localization bursts coordinate gene regulation. *Nature* 455, 485–490.
- Calnan, D.R., and Brunet, A. (2008). The FoxO code. *Oncogene* 27, 2276–2288.
- Chen, J.Y., Lin, J.R., Cimprich, K.A., and Meyer, T. (2012). A two-dimensional ERK-AKT signaling code for an NGF-triggered cell-fate decision. *Mol. Cell* 45, 196–209.
- Cheong, R., Rhee, A., Wang, C.J., Nemenman, I., and Levchenko, A. (2011). Information transduction capacity of noisy biochemical signaling networks. *Science* 334, 354–358.
- Coleman, T.F., and Li, Y. (1996). An interior trust region approach for nonlinear minimization subject to bounds. *SIAM J. Optimization* 6, 418–445.
- De Boor, C. (2001). *A Practical Guide to Splines* (Springer).
- Eijkelenboom, A., and Burgering, B.M. (2013). FOXOs: signalling integrators for homeostasis maintenance. *Nat. Rev. Mol. Cell Biol.* 14, 83–97.
- Elowitz, M.B., and Leibler, S. (2000). A synthetic oscillatory network of transcriptional regulators. *Nature* 403, 335–338.
- Essers, M.A., Weijzen, S., de Vries-Smits, A.M., Saarloos, I., de Ruiter, N.D., Bos, J.L., and Burgering, B.M. (2004). FOXO transcription factor activation by oxidative stress mediated by the small GTPase Ral and JNK. *EMBO J.* 23, 4802–4812.
- Friedman, N., Linal, M., Nachman, I., and Pe'er, D. (2000). Using Bayesian networks to analyze expression data. *J. Comput. Biol.* 7, 601–620.
- Friedman, N., Murphy, K., and Russell, S. (1998). Learning the structure of dynamic probabilistic networks. In *Proceedings of the Fourteenth Conference on Uncertainty in Artificial Intelligence*, G.F. Cooper and S. Moral, eds. (Morgan Kaufmann), pp. 139–147.
- Geiger, D., and Heckerman, D. (1994). Learning Gaussian networks. In *Proceedings of the Tenth International Conference on Uncertainty in Artificial Intelligence*, R. Lopez De Mantaras and D. Poole, eds. (Morgan Kaufmann), pp. 235–243.
- Greer, E.L., Oskoui, P.R., Banko, M.R., Maniar, J.M., Gygi, M.P., Gygi, S.P., and Brunet, A. (2007). The energy sensor AMP-activated protein kinase directly regulates the mammalian FOXO3 transcription factor. *J. Biol. Chem.* 282, 30107–30119.
- Gross, S.M., and Rotwein, P. (2015). Akt signaling dynamics in individual cells. *J. Cell Sci.* 128, 2509–2519.
- Grzegorzczak, M. (2010). An introduction to Gaussian Bayesian networks. *Methods Mol. Biol.* 662, 121–147.
- Halford, D., Shoaf, J.H., and Riskey, A.S. (1973). Spectral Density Analysis: Frequency Domain Specification Measurement Signal. Stability. 27th Annual Symposium on Frequency Control, 421–431.
- Hansen, A.S., and O’Shea, E.K. (2015). Limits on information transduction through amplitude and frequency regulation of transcription factor activity. *eLife* 4, <https://doi.org/10.7554/eLife.06559>.
- Hansen, A.S., and O’Shea, E.K. (2016). Encoding four gene expression programs in the activation dynamics of a single transcription factor. *Curr. Biol.* 26, R269–R271.
- Hao, N., and O’Shea, E.K. (2011). Signal-dependent dynamics of transcription factor translocation controls gene expression. *Nat. Struct. Mol. Biol.* 19, 31–39.
- Hausdorff, J.M., and Peng, C. (1996). Multiscaled randomness: a possible source of 1/f noise in biology. *Phys. Rev. E Stat. Phys. Plasmas Fluids Relat. Interdiscip. Top.* 54, 2154–2157.

- Heckerman, D., Geiger, D., and Chickering, D.M. (1995). Learning bayesian networks: the combination of knowledge and statistical data. *Machine Learn.* 20, 197–243.
- Hill, S.M., Lu, Y., Molina, J., Heiser, L.M., Spellman, P.T., Speed, T.P., Gray, J.W., Mills, G.B., and Mukherjee, S. (2012). Bayesian inference of signaling network topology in a cancer cell line. *Bioinformatics* 28, 2804–2810.
- Hu, M.C., Lee, D.F., Xia, W., Golfman, L.S., Ou-Yang, F., Yang, J.Y., Zou, Y., Bao, S., Hanada, N., Saso, H., et al. (2004). IkkappaB kinase promotes tumorigenesis through inhibition of forkhead FOXO3a. *Cell* 117, 225–237.
- Huang, H., Regan, K.M., Lou, Z., Chen, J., and Tindall, D.J. (2006). CDK2-dependent phosphorylation of FOXO1 as an apoptotic response to DNA damage. *Science* 314, 294–297.
- Jensen, K.S., Binderup, T., Jensen, K.T., Therkelsen, I., Borup, R., Nilsson, E., Multhaupt, H., Bouchard, C., Quistorff, B., Kjaer, A., et al. (2011). FoxO3A promotes metabolic adaptation to hypoxia by antagonizing Myc function. *EMBO J.* 30, 4554–4570.
- Kamentsky, L., Jones, T.R., Fraser, A., Bray, M.A., Logan, D.J., Madden, K.L., Ljosa, V., Rueden, C., Eliceiri, K.W., and Carpenter, A.E. (2011). Improved structure, function and compatibility for CellProfiler: modular high-throughput image analysis software. *Bioinformatics* 27, 1179–1180.
- Kellogg, R.A., and Tay, S. (2015). Noise facilitates transcriptional control under dynamic inputs. *Cell* 160, 381–392.
- Komatsu, N., Aoki, K., Yamada, M., Yukinaga, H., Fujita, Y., Kamioka, Y., and Matsuda, M. (2011). Development of an optimized backbone of FRET biosensors for kinases and GTPases. *Mol. Biol. Cell* 22, 4647–4656.
- Kraskov, A., Stögbauer, H., and Grassberger, P. (2004). Estimating mutual information. *Phys. Rev. E Stat. Nonlin. Soft Matter Phys.* 69, 066138.
- Kreutz, C., Bartolome Rodríguez, M.M., Maiwald, T., Seidl, M., Blum, H.E., Mohr, L., and Timmer, J. (2007). An error model for protein quantification. *Bioinformatics* 23, 2747–2753.
- Lahav, G., Rosenfeld, N., Sigal, A., Geva-Zatorsky, N., Levine, A.J., Elowitz, M.B., and Alon, U. (2004). Dynamics of the p53-Mdm2 feedback loop in individual cells. *Nat. Genet.* 36, 147–150.
- Lehtinen, M.K., Yuan, Z., Boag, P.R., Yang, Y., Villen, J., Becker, E.B., DiBacco, S., de la Iglesia, N., Gygi, S., Blackwell, T.K., et al. (2006). A conserved MST-FOXO signaling pathway mediates oxidative-stress responses and extends life span. *Cell* 125, 987–1001.
- Lev Bar-Or, R., Maya, R., Segel, L.A., Alon, U., Levine, A.J., and Oren, M. (2000). Generation of oscillations by the p53-Mdm2 feedback loop: a theoretical and experimental study. *Proc. Natl. Acad. Sci. USA* 97, 11250–11255.
- Levine, J.H., Lin, Y., and Elowitz, M.B. (2013). Functional roles of pulsing in genetic circuits. *Science* 342, 1193–1200.
- Li, Z., Kowitsch, A., Zhou, G., Groth, T., Fuhrmann, B., Niepel, M., Amado, E., and Kressler, J. (2013). Enantiopure chiral poly(glycerol methacrylate) self-assembled monolayers knock down protein adsorption and cell adhesion. *Adv. Healthc. Mater.* 2, 1377–1387.
- Lin, Y., Sohn, C.H., Dalal, C.K., Cai, L., and Elowitz, M.B. (2015). Combinatorial gene regulation by modulation of relative pulse timing. *Nature* 527, 54–58.
- Moelling, K., Schad, K., Bosse, M., Zimmermann, S., and Schwenecker, M. (2002). Regulation of Raf-Akt cross-talk. *J. Biol. Chem.* 277, 31099–31106.
- Murphy, K.P. (2002). *Dynamic Bayesian Networks: Representation, Inference and Learning* (University of California, Berkeley), p. 268.
- Nam, H.S., and Benezra, R. (2009). High levels of Id1 expression define B1 type adult neural stem cells. *Cell Stem Cell* 5, 515–526.
- Neapolitan, R.E. (2004). *Learning Bayesian Networks* (Pearson Prentice Hall).
- Nelson, D.E., Ihekwaba, A.E., Elliott, M., Johnson, J.R., Gibney, C.A., Foreman, B.E., Nelson, G., See, V., Horton, C.A., Spiller, D.G., et al. (2004). Oscillations in NF-kappaB signaling control the dynamics of gene expression. *Science* 306, 704–708.
- Niepel, M., Hafner, M., Pace, E.A., Chung, M., Chai, D.H., Zhou, L., Muhlich, J.L., Schoeberl, B., and Sorger, P.K. (2014). Analysis of growth factor signaling in genetically diverse breast cancer lines. *BMC Biol.* 12, 20.
- Novak, B., and Tyson, J.J. (2008). Design principles of biochemical oscillators. *Nat. Rev. Mol. Cell Biol.* 9, 981–991.
- Otsu, N. (1979). A threshold selection method from gray-level histograms. *IEEE Trans. Syst. Man Cybern.* 9, 62–66.
- Porter, J.R., Fisher, B.E., and Batchelor, E. (2016). p53 pulses diversify target gene expression dynamics in an mRNA half-life-dependent manner and delineate Co-regulated target gene subnetworks. *Cell Syst.* 2, 272–282.
- Purvis, J.E., Karhohs, K.W., Mock, C., Batchelor, E., Loewer, A., and Lahav, G. (2012). p53 dynamics control cell fate. *Science* 336, 1440–1444.
- Purvis, J.E., and Lahav, G. (2013). Encoding and decoding cellular information through signaling dynamics. *Cell* 152, 945–956.
- Ramsay, J.O., Hooker, G., and Graves, S. (2009). *Functional Data Analysis with R and MATLAB* (Springer).
- Ramsay, J.O., and Silverman, B.W. (2005). *Functional Data Analysis, Second Edition* (Springer).
- Schilling, M., Maiwald, T., Bohl, S., Kollmann, M., Kreutz, C., Timmer, J., and Klingmüller, U. (2005). Computational processing and error reduction strategies for standardized quantitative data in biological networks. *FEBS J.* 272, 6400–6411.
- Senapedis, W.T., Kennedy, C.J., Boyle, P.M., and Silver, P.A. (2011). Whole genome siRNA cell-based screen links mitochondria to Akt signaling network through uncoupling of electron transport chain. *Mol. Biol. Cell* 22, 1791–1805.
- Sparta, B., Pargett, M., Minguet, M., Distor, K., Bell, G., and Albeck, J.G. (2015). Receptor level mechanisms are required for epidermal growth factor (EGF)-stimulated extracellular signal-regulated kinase (ERK) activity pulses. *J. Biol. Chem.* 290, 24784–24792.
- Tay, S., Hughey, J.J., Lee, T.K., Lipniacki, T., Quake, S.R., and Covert, M.W. (2010). Single-cell NF-kappaB dynamics reveal digital activation and analogue information processing. *Nature* 466, 267–271.
- Timmer, J., Haussler, S., Lauk, M., and Lücking, C.H. (2000). Pathological tremors: deterministic chaos or nonlinear stochastic oscillators? *Chaos* 10, 278–288.
- Tran, H., Brunet, A., Grenier, J.M., Datta, S.R., Fornace, A.J., Jr., DiStefano, P.S., Chiang, L.W., and Greenberg, M.E. (2002). DNA repair pathway stimulated by the forkhead transcription factor FOXO3a through the Gadd45 protein. *Science* 296, 530–534.
- Traverse, S., Seedorf, K., Paterson, H., Marshall, C.J., Cohen, P., and Ullrich, A. (1994). EGF triggers neuronal differentiation of PC12 cells that overexpress the EGF receptor. *Curr. Biol.* 4, 694–701.
- van der Horst, A., and Burgering, B.M. (2007). Stressing the role of FoxO proteins in lifespan and disease. *Nat. Rev. Mol. Cell Biol.* 8, 440–450.
- Yang, J.Y., Zong, C.S., Xia, W., Yamaguchi, H., Ding, Q., Xie, X., Lang, J.Y., Lai, C.C., Chang, C.J., Huang, W.C., et al. (2008). ERK promotes tumorigenesis by inhibiting FOXO3a via MDM2-mediated degradation. *Nat. Cell Biol.* 10, 138–148.
- Yu, C.F., Liu, Z.X., and Cantley, L.G. (2002). ERK negatively regulates the epidermal growth factor-mediated interaction of Gab1 and the phosphatidylinositol 3-kinase. *J. Biol. Chem.* 277, 19382–19388.

## STAR★METHODS

### KEY RESOURCES TABLE

REAGENT or RESOURCE	SOURCE	IDENTIFIER
<b>Antibodies</b>		
Rabbit monoclonal anti-phospho-p44/p42 (Thr202/Tyr204) (D13.14.4E)	Cell Signaling (CST)	Cat#4370; RRID: AB_2315112
Rabbit monoclonal anti-phospho-Akt (Ser473) (D9E)	Cell Signaling (CST)	Cat#4060; RRID: AB_2315049
Rabbit polyclonal anti-phospho-FoxO3a (Ser253)	Cell Signaling (CST)	Cat#9466; RRID: AB_2106674
Rabbit polyclonal anti-phospho-FoxO3a (Ser294)	Cell Signaling (CST)	Cat#5538; RRID: AB_10696878
Rabbit monoclonal anti-FoxO3a (75D8)	Cell Signaling (CST)	Cat#2497; RRID: AB_836876
Mouse monoclonal anti- $\beta$ -Actin (Clone AC-74)	Sigma-Aldrich	Cat#A2228; RRID: AB_476697
Goat polyclonal anti-Rabbit IgG (H+L) conjugated with Alexa Fluor 680	Thermo Fisher	Cat#A32734; RRID: AB_2633283
Goat polyclonal anti-Mouse IgG (H+L) conjugated with Alexa Fluor 800	Thermo Fisher	Cat#A32730; RRID: AB_2633279
<b>Chemicals, Peptides, and Recombinant Proteins</b>		
Recombinant Human Epidermal growth factor	PeproTech	Cat#AF-100-15
Recombinant Human Betacellulin	PeproTech	Cat#100-50
Recombinant Human Epiregulin	PeproTech	Cat#100-04
Recombinant Human HGF	PeproTech	Cat#100-39
Recombinant Human Heregulin	PeproTech	Cat#100-03
Recombinant Human IGF-1	PeproTech	Cat#AF-100-11
MK-2206 AKT1/2/3 inhibitor	Selleck Chemicals	Cat#S1078
Cholera Toxin	Sigma-Aldrich	Cat#C8052
Hydrocortisone	Sigma-Aldrich	Cat#H0888
Insulin	Sigma-Aldrich	Cat#I9278
Bovine Serum Albumin	Sigma-Aldrich	Cat#A7906
Heat Inactivated Horse Serum	Life Technologies	Cat#26050
Puromycin	Life Technologies	Cat#A113803
Fugene HD	Promega	Cat#E2311
DMEM/F-12 1:1	Life Technologies	Cat#11320
CI-1040 MEK1/2 inhibitor	Selleck Chemicals	Cat#S1020
PD0325901 MEK1/2 inhibitor	Selleck Chemicals	Cat#S1036
<b>Critical Commercial Assays</b>		
Gibson Assembly	New England BioLabs	E2611
<b>Deposited Data</b>		
Raw images	This paper; OMERO	<a href="http://lincs.hms.harvard.edu/sampattavanich-cellsyst-2018/">http://lincs.hms.harvard.edu/sampattavanich-cellsyst-2018/</a>
Raw data for generating all plots in the paper	This paper	<a href="http://dx.doi.org/10.17632/65fkdzt9x5.1">http://dx.doi.org/10.17632/65fkdzt9x5.1</a>
<b>Experimental Models: Cell Lines</b>		
184A1	ATCC	ATCC CRL-8798; RRID:CVCL_3040
MCF10A	ATCC	ATCC CRL-10317; RRID:CVCL_0598
HCC1806	ATCC	ATCC CRL-2335; RRID:CVCL_1258
BT-20	ATCC	ATCC HTB-19; RRID:CVCL_0178
MDA-MB-231	ATCC	ATCC HTB-26; RRID:CVCL_0062
T47D	ATCC	ATCC HTB-133; RRID:CVCL_0553
Hs578T	ATCC	ATCC HTB-126; RRID:CVCL_0332

(Continued on next page)

<b>Continued</b>		
REAGENT or RESOURCE	SOURCE	IDENTIFIER
MCF7	ATCC	ATCC HTB-22; RRID:CVCL_0031
SKBR3	ATCC	ATCC HTB-30;RRID:CVCL_0033
<b>Oligonucleotides</b>		
EKAREV-forward PCR primer : CTGTCTCATCATTTT GGCAAAG	This paper	N/A
EKAREV-reverse PCR primer : CACGTGCGCCGGCCT GCTTCAGCAGGCTGAAGTTGGTGGCGCCGCTGCC ATCCAGAGTCAGGCGTTCC	This paper	N/A
mCherry-forward PCR primer: CCCATACGATGTTCCAGATTACGCTGGAGGATCCG GGGGTTCTATGGTGAGCAAGGGCGAGG	This paper	N/A
mCherry-reverse PCR primer: CTGACACACATTCCACAGGGTCGACTTACTTGTACAG CTCGTCCATG	This paper	N/A
F3aN400-forward PCR primer: TTCAGCCTGCTGAAGC AGGCCGGCGACGTGGAGGAGAACCCCGGCCCAT GGCCGAAGCCCCC	This paper	N/A
F3aN400-reverse PCR primer: CTCCAGCGTAATCTGGAACATC	This paper	N/A
<b>Recombinant DNA</b>		
Plasmid: pPB-CAG-EKAREV	(Albeck et al., 2013; Komatsu et al., 2011)	N/A
Plasmid: pMSCV-puro-F3aN400-Venus	This paper	Pending for submission to Addgene
Plasmid: pPB-CAG-F3aN400-HA-Venus-P2A-NLS- Myc-mCherry	This paper	Pending for submission to Addgene
Plasmid: pPB-CAG-EKAREV-P2A-F3aN400-HA-mCherry	This paper	Pending for submission to Addgene
Plasmid: ERK-silent F3aN400-HA-Venus (with S294A/S344A)	This paper	Pending for submission to Addgene
Plasmid: an AKT-silent F3aN400-HA-Venus (with T32A/S253A/S315A)	This paper	Pending for submission to Addgene
Plasmid: pPB-CAG.EBNXN	A. Bradley, Sanger Institute	N/A
Plasmid: pCMV-hyPBase transposase vector	A. Bradley, Sanger Institute	N/A
Plasmid: pcDNA3-H2B-mCherry	(Nam and Benezra, 2009)	Addgene Plasmid#20972
<b>Software and Algorithms</b>		
Scripts for all quantitative analysis in this paper	This paper	<a href="https://github.com/sorgerlab/sampattavanich-cellsyst-2018">https://github.com/sorgerlab/ sampattavanich-cellsyst-2018</a>
Functional data analysis MATLAB package	J. Ramsay	<a href="http://www.psych.mcgill.ca/misc/fda/&lt;br/&gt;downloads/FDAfuns/Matlab/">http://www.psych.mcgill.ca/misc/fda/ downloads/FDAfuns/Matlab/</a>
MATLAB	Mathworks	N/A
CellProfiler	(Kamentsky et al., 2011)	<a href="http://cellprofiler.org/">http://cellprofiler.org/</a>
<b>Other</b>		
Resource website for data public sharing of LINC5 compatible dataset	This paper	<a href="http://lincs.hms.harvard.edu/&lt;br/&gt;sampattavanich-cellsyst-2018/">http://lincs.hms.harvard.edu/ sampattavanich-cellsyst-2018/</a>

## CONTACT FOR REAGENT AND RESOURCE SHARING

Further information and requests for resources and reagents should be directed to and will be fulfilled by the Lead Contact, Peter Sorger ([peter\\_sorger@hms.harvard.edu](mailto:peter_sorger@hms.harvard.edu)).

## EXPERIMENTAL MODEL AND SUBJECT DETAILS

### Tissue Culture Cell Lines

The different cell lines were obtained from the following sources: 184A1 (ATCC® CRL-8798) from ATCC; MCF10A (ATCC® CRL-10317) from ATCC; HCC1806(ATCC® CRL-2335) from ATCC; BT-20 (ATCC® HTB-19) from ATCC; MDA-MB-231 (ATCC® HTB-26) from ATCC; T47D (ATCC® HTB-133) from ATCC; Hs578T (ATCC® HTB-126) from ATCC; MCF7 (ATCC® HTB-22) from ATCC; SKBR3 (ATCC® HTB-30) from ATCC. All cells were quarantined before they were used for experiments and were tested for mycoplasma and other microbial contamination. All cell lines were authenticated by profiling highly-polymorphic short tandem repeat loci (STRs) by the Dana Farber Cancer Institute (DFCI) Molecular Diagnostics Laboratory. The sex of the cell lines are as follows; Female:184A1, MCF10A, HCC1806, BT-20, MDA-MB-231, T47D, Hs578T, MCF7, SKBR3. MCF-10A and 184A1 cells were cultured at 37°C with 5% CO<sub>2</sub> in DMEM/F12 (Invitrogen) supplemented with 5% horse serum, 20 ng/mL EGF, 10 µg/mL insulin, 0.5 µg/mL hydrocortisone, 100 ng/mL cholera toxin, 50 U/mL penicillin and 50 µg/mL streptomycin; all other cells were grown according to ATCC recommendations.

## METHOD DETAILS

### Tissue Culture

For experiments involving growth factor stimulation cells were plated and cultured in full growth media for 24 hours. At time of experiment, cells were washed twice with PBS and then placed in serum-free medium (DMEM/F12 with Penicillin/Streptomycin but no phenol red) for 5 hr, followed by washing and replenishing in fresh serum-free medium for 1hr. Cells were then exposed to growth-factors in serum-free medium, resulting in a ~5% volume increase. In experiments with kinase inhibitors, drugs were added 1 hr prior to growth factors, unless indicated otherwise.

### Construction of Plasmids and Reporter Cell Line Establishment

The complete coding sequence of human FoxO3 was inserted into pBabe-puro upstream of mVenus and an H212R mutation introduced into the DNA binding domain (Tran et al., 2002). When transduced into MCF10A cells with retroviruses, this construct translocated into the cytosol upon insulin treatment. However, expression levels were uneven among clonal cell populations and cells grew poorly. Thus, a region of FoxO3-H212R corresponding to amino acid residues 1-400 was inserted into pMSCV-puro, upstream of a Venus sequence, to generate pMSCV-puro-F3aN400-Venus. When introduced stably into MCF-10A cells by retroviral transduction, this construct displayed translocation from the nucleus to the cytosol upon insulin treatment, and translocation to the nucleus in response to inhibitors of AKT or PI3K.

To clone fluorescently tagged FoxO3 constructs containing mutations at known sites of phosphorylation a pUC57 plasmid was designed and synthesized by GENEWIZ (Figure S8A), containing an ERK-silent F3aN400-FLAG-mCerulean (with S294A/S344A mutations in FoxO3 sequences), an AKT-silent F3aN400-HA-Venus (with T32A/S253A/S315A in FoxO3 sequences and an NLS-Myc-mCherry, separated by self-cleaving P2A sites. Silent mutations were introduced to create unique restriction sites for generating the following constructs: ERK-silent F3aN400-HA-Venus-P2A-NLS-Myc-mCherry (NaeI) (Figure S8B) or AKT-silent F3aN400-HA-Venus-P2A-NLS-Myc-mCherry (XhoI). To create a FoxO3 construct without AKT- or ERK-specific mutations (F3aN400-HA-Venus-P2A-NLS-Myc-mCherry) from this synthetic construct, a PCR fragment from wildtype-FoxO3 was introduced into the NotI/NaeI sites of ERK-silent F3aN400-HA-Venus-P2A-NLS-Myc-mCherry. All FoxO3 constructs were subsequently subcloned into the EcoRI/Sall restriction sites of pPB-CAG.EBNXN (A. Bradley, Sanger Institute) containing a puromycin selection cassette.

To create the dual reporter construct pPB-CAG-EKAREV-P2A-F3aN400-HA-mCherry containing the ERK reporter EKAREV (Albeck et al., 2013; Komatsu et al., 2011) and a F3aN400-mCherry separated by a self-cleaving P2A site, PCR fragments were generated from pPB-CAG-EKAREV using the EKAREV primer pairs, pPB-CAG-F3aN400-HA-Venus-P2A-NLS-Myc-mCherry using the F3aN400 primer pairs and pcDNA3-H2B-mCherry, Addgene plasmid 20972 (Nam and Benezra, 2009) using the mCherry primer pairs (Key Resources Table) were cloned into the EcoRI/Sall restriction sites of pPB-CAG-EKAREV using Gibson Assembly (New England BioLabs).

To create stable cell lines and minimize recombination between highly similar fluorescent protein sequences, piggyBac transposon-mediated gene transfer was used; the pPB-CAG expression vectors were co-transfected with a pCMV-hyPBBase transposase vector (A. Bradley, Sanger Institute). All FoxO3 sensors were co-expressed with the nuclear reporter NLS-mCherry to facilitate image segmentation, either by double delivery using retroviral infection or by joining the nuclear reporter with the FoxO3 sensor using the P2A ribosomal skipping sequence.

### Analysis of Total Cellular Lysates

Cells grown and starved as described above were lysed using RIPA-Buffer (Sigma) supplemented with Complete Protease Inhibitor Cocktail (Roche) with sonication on ice. Extracts were analyzed using SDS-Page followed by transfer to PVDF membranes (Millipore), blocking with Odyssey Blocking Buffer (LI-COR) for 1h, washing with PBS/0.1% Tween and incubation with primary antibody overnight at 4°C in Odyssey Blocking Buffer. Blots were developed and scanned following the Odyssey protocol (LI-COR).

### Fixed and Live-Cell Microscopy

For live time-lapse microscopy, cells expressing reporter constructs were plated in 96-well plates at  $\sim 6 \times 10^5$  cells/cm<sup>2</sup> and then imaged using a 10x objective on a Nikon Eclipse inverted fluorescence microscope fitted with an environmental chamber maintained at 37°C with 5% CO<sub>2</sub>. Images were collected at 5–10 minutes intervals for a period of 24 hr using the Hamamatsu ORCA-ER cooled CCD camera and Spectra-X light engine (Lumencor). Filter sets used in this study included the polychroic mirror (251050, Chroma), CFP (Ex:440/20, Em:475/20), FRET (Ex:440/20, Em:540/21), YFP (Ex:508/24, Em:540/21) and RFP (Ex:575/22, Em:632/60).

For fixed cell assays for immunostaining, cells were fixed for 10 minutes at room temperature with 2% paraformaldehyde in PBS and then permeabilized with 100% methanol for 10 minutes. After blocking with Odyssey blocking buffer (LI-COR) for 1 hour, cells were incubated with primary antibodies overnight at 4°C. Samples were washed, stained with secondary antibodies at room temperature for 1 hour and counter-stained with DAPI and a whole cell stain (Thermo Scientific) at room temperature for 1 hour. After washing, plates were imaged at 10X using an Operetta high-content imaging system (Perkin Elmer).

## QUANTIFICATION AND STATISTICAL ANALYSIS

### Calculation of FoxO3 Translocation Activity

For fixed immunostained cells, image segmentation was performed using cellProfiler (Kamentsky et al., 2011) and extracted features analyzed using MATLAB scripts. For live imaging, cell tracking and segmentation were performed using MATLAB scripts. Image segmentation was performed on the nuclear image of each field using NLS-mCherry signal. Cell tracking was performed by cross-correlation between adjacent frames and validated manually. To calculate FoxO3 translocation dynamics, we first identified nuclear compartment of each cell using either DAPI staining of fixed cells or the NLS-mCherry channel for live microscopy. We then determined the cell boundary either by thresholding to detect the outer cell boundary or by expanding 4 pixels from the nuclear boundary (Figure S1A). We quantified FoxO3 translocation by calculating the ratio between the mean pixel intensity in the cytosolic and nuclear compartments (C/N). For fixed cell studies, FoxO3 intensity was determined by immunostaining cell with anti-FoxO3 antibody. For live microscopy, FoxO3 intensity was derived from direct imaging of the F3aN400 reporter. We often report FoxO3 C/N ratios as log base 10 transformed values ( $\log_{10}(C/N)$ ) so that trajectories with equal FoxO3 intensity inside the nuclear and the cytosolic compartments are centered at 0. To minimize variability in background fluorescence arising from variation in light source or camera drift over time, we first subtracted the mean pixel values in each compartment by the mean pixel value of the background, followed by calculating the log base 10 ratios; this gives rise to the normalized ratio  $\log_{10}(C_{norm}/N_{norm})$  (Figure S1A). For EKAREV, the background signal was first subtracted, and the FRET/CFP ratio calculated at the single pixel level. ERK activity was then calculated from the mean value from the cytosolic compartment of the normalized FRET/CFP values.

### Scaling of Western Blots; Error Propagation; Total Least Squares

Protein concentrations were estimated using Western blotting; each measurement (e.g. pAkt<sup>S473</sup> intensity from blotting) was normalized to its maximum value across an entire experiment. To account for systematic variation within each gel, the intensity of actin staining was used as a calibration standard (Schilling et al., 2005). The following computational analysis was performed to obtain a merged data set. For Immunoblotting, measurement noise is usually log-normal distributed (Kreutz et al., 2007) hence data was log-transformed. Observations from multiple experiments were merged by assigning each data-point  $y_{obs}(c_{ij}, t_{ik})$  for condition  $c_{ij}$  and timepoint  $t_{ik}$  a common scaling factor  $\hat{s}_i$  for each observable and experiment, i.e.  $\hat{y}_{ijk} = \hat{s}_i \cdot y_{obs}(c_{ij}, t_{ik})$ , or

$$y_{ijk} = s_i + \log_2(y_{obs}(c_{ij}, t_{ik})) \quad (\text{Equation 1})$$

in the log space. Different gels performed within a single experiment were assumed to be comparable and therefore assigned the same scaling factors. For  $N$  experiments, there are  $N-1$  degrees of freedom in terms of scaling; therefore,  $s_1$  was set to 1 without loss of generality. To merge data-sets from multiple experiments, the objective function

$$RSS_1 = \sum_{i,j,k} (y_m(c_j, t_k) - y_{ijk})^2 \quad (\text{Equation 2})$$

was minimized, yielding the maximum likelihood estimates

$$(s_i^*, y^*(c_j, t_k)) = \underset{i}{\operatorname{argmin}} RSS_1 \quad (\text{Equation 3})$$

for scaling factors  $s_i^*$  and merged values  $y^*(c_j, t_k)$ . For numerical optimization of  $RSS_1$ , the MATLAB function *lsqnonlin* was applied using the trust-region method (Coleman and Li, 1996). Using the Jacobian matrix  $J$ , we then calculated the uncertainty of estimates from

$$\sigma = \sqrt{\operatorname{diag}(J^T J)^{-1}}. \quad (\text{Equation 4})$$

Ratios (or differences in log-space) of the merged values

$$r_{jlk} = y^*(c_j, t_k) - y^*(c_l, t_k) \quad (\text{Equation 5})$$

were calculated as final readout of the analysis. Uncertainties were propagated using the following equation:

$$\sigma(r_{jlk}) = \sqrt{\sigma(y^*(c_j, t_k))^2 + \sigma(y^*(c_i, t_k))^2}. \quad (\text{Equation 6})$$

Equation 6 was used to determine propagated errors for the pERK/pAKT ratios in Figure 1C. For any indexed sets  $M = \{jlk_1, jlk_2, \dots, jlk_M\}$  and  $Q = \{opq_1, opq_2, \dots, opq_M\}$  with samples that share a linear relationship, we assume a linear model  $a \cdot x + b$  for the relationship of  $(r_M, r_Q)$ , and can apply total least squares to determine estimates and uncertainties of both dependent and independent variables simultaneously. For this purpose, the following objective function

$$RSS_2 = \sum_{M,Q} \frac{1}{\sigma(r_{jlk})} \left( r_{jlk} - \frac{r_{opq} - b}{a} \right) + \frac{1}{\sigma(r_{opq})} (r_{opq} - a \cdot r_{opq} - b) \quad (\text{Equation 7})$$

was numerically optimized as discussed in Equation 3. Using this formula, the constraint of relative data having an unknown scaling factor with respect to concentration level does not influence the slope  $a$ , but only offsetting  $b$ .

Different experiments are scaled in reference with each other, resulting in merged  $y^*$  and corresponding uncertainties. Ratios of normalized parameters were then calculated. In our study (Figure 1C), we applied this approaches to the ratios of pERK/pAKT and pS294/pS253, and a linear model was fitted to their relationship using total least squares.

### Functional Principal Component Analysis (fPCA)

To analyze the underlying trends of the reporter translocation trajectories, we implemented functional principal component analysis (fPCA). Similar to classical principal component analysis, this technique generates an empirical set of orthogonal basis functions  $\psi_i(t)$  that comply with

$$\langle \psi_i, \psi_j \rangle = \int \psi_i(t) \psi_j(t) dt = 0 \quad (\text{Equation 8})$$

and these basis functions also yield maximal variance for any  $i \neq j$ . We first applied this technique for the early synchronous response, with  $t \in [-70, 80]$  min. Equidistantly spaced cubic b-splines (De Boor, 2001) were used to convert the input signals to continuous time-courses. We smoothed the signals using 1.5 data-points per basis function to avoid overfitting. Artifacts at the edges, normally arising at the beginning and at the end of each trajectory, were not an issue here because of the high number of trajectories for basis calculation (total of over 5000 trajectories). Using the implementation described by Ramsay (Ramsay et al., 2009; Ramsay and Silverman, 2005), we identified three orthonormal basis functions (harmonics) that together explain over 95% of the observed variance. To make biological senses of the observed basis functions, we rotated the three basis functions using the following transformation:

$$R = \begin{pmatrix} 1 & 0 & 0 \\ 0 & \cos\theta_3 & \sin\theta_3 \\ 0 & -\sin\theta_3 & \cos\theta_3 \end{pmatrix} \begin{pmatrix} \cos\theta_2 & 0 & -\sin\theta_2 \\ 0 & 1 & 0 \\ \sin\theta_2 & 0 & \cos\theta_2 \end{pmatrix} \begin{pmatrix} \cos\theta_1 & \sin\theta_1 & 0 \\ -\sin\theta_1 & \cos\theta_1 & 0 \\ 0 & 0 & 1 \end{pmatrix} \quad (\text{Equation 9})$$

using Euler angles  $\theta_1 = -25^\circ$ ,  $\theta_2 = 5^\circ$  and  $\theta_3 = -5^\circ$ . The first harmonic fPC1 corresponds to a steady-state value prior to ligand addition and is not significantly different between growth factor stimuli (Figure 3C). The second harmonic fPC2 corresponds to a sustained translocation starting at  $t=0$  min and the third harmonic fPC3 corresponds to a transient function that falls below baseline at  $t=60$  min. For  $t > 80$  min, all harmonics converge to the Fourier basis, implying that trajectories from late-response are truly asynchronous.

### Pulse Score and Fraction of Pulsing Cells

Trajectory artifacts such as spikes resulting from cell division or loss of cell tracking were first removed by interpolation. Missing values were added by interpolation for fPCA and dropped in subsequent analysis. For F3aN400-Venus translocation trajectories, the first three fPCA harmonics were employed to detrend the signals (as shown in Figure 4A) and an additive model of slow trend and fast pulsing assumed. The detrended signal was smoothed using  $N/3$  bsplines for  $N$  data points. For EKAREV traces, an averaged trend determined from average sliding window was first applied to detrend the signal. Peaks were then detected on smoothed and detrended trajectories. Due to overfitting, pulsatile traces often contain small peaks. We dropped small peaks with edge height less than 0.005. The final detrended, interpolated, and peak adjusted signals were used for detecting edges that connect from peak to peak of each trajectory. As a result, we can define edges into two finite sets:  $T_{\text{start}} = \{t_{s(1)}, \dots, t_{s(N_{\text{edge}})}\}$  and  $T_{\text{end}} = \{t_{e(1)}, \dots, t_{e(N_{\text{edge}})}\}$ , depicting the starting and ending points of all edges, respectively. The index set  $\mathcal{I} \subset \{1, \dots, N_{\text{edge}}\}$  with  $N_{\mathcal{I}}$  elements contains indices of edges that are directly connected to a neighboring edge. Superscripts + and - denote ascending and descending edges and  $N_{\text{peak}}$  the total number of peaks. The deviation of the smoothed signal  $y$  and data  $y^D$  is quantified with  $RSS = \sum_{k=1}^N (y(t_k) - y^D(t_k))^2$ .

For calculating the pulse score, the following features  $f_i$  were extracted (See also Figure 4A)

1. Number of pulse edges:  $f_1 = N_{\text{edge}} \approx 2N_{\text{peak}}$
2. Pulse amplitude:  $f_2 = \max \tilde{y}(t) - \min \tilde{y}(t)$
3. Signal to noise ratio:  $f_3 = \frac{f_2}{1/(N-1)\sqrt{RSS}}$

$$4. \text{ Peak duration: } f_4 = \frac{1}{N_I} \sum_{i \in \mathcal{I}} |t_{s(i)} - t_{e(i+1)}|$$

$$5. \text{ Peak distance: } f_5 = \frac{1}{N_{\text{edge}} - 1} \sum_{i=1}^{N_{\text{edge}}-1} |t_{s(i+1)}^\pm - t_{s(i)}^\pm| + \frac{1}{N_{\text{edge}} - 1} \sum_{i=1}^{N_{\text{edge}}-1} |t_{e(i+1)}^\pm - t_{e(i)}^\pm|$$

Whenever no peaks were detected, peak duration and peak distance were set to 300 min. A reference value  $r_i$  and a set of weights  $w_i$  was defined for all features  $f_i$ . Positive values for  $w_i$  represent features for which a larger value corresponds to more pulsing, i.e. number of edges, amplitude, and signal to noise ratio. Respectively, a negative number for  $w_i$  depicts a feature for which a larger value indicates less pulsing, namely peak duration and peak distance. Using the features  $f_i$ , the reference values  $r_i$ , and the weights  $w_i$ , the pulsatory score was calculated for each trajectory based on the following formula:

$$p = \prod_i \left( \frac{f_i}{r_i} \right)^{w_i}. \quad (\text{Equation 10})$$

Reference values and weights were adjusted by sorting trajectories by their pulse score  $p$  to achieve visual ordering of pulsing. Resulted reference values and weights are  $r = (90, 0.04, 40, 300, 300)$  and  $w = (2, 1, 1.5, -1.5, -1.5)$ , for all five characteristics of pulse score, respectively. A threshold pulse score of 0.6 was used for assigning each trajectory into the pulsing or non-pulsing groups. The choice of 0.6 was supported by visual inspection that this threshold can best separate BTC-stimulated cells from IGF1-stimulated condition (Figure 4A). Finally, the fraction of pulsing cells was calculated for each condition based on

$$\text{fp} = \frac{N_{\text{pulsing}}}{N_{\text{all}}}. \quad (\text{Equation 11})$$

### Power Spectrum Analysis

Time-course measurements from single cells were ordered according to their pulsatory score and subsequently grouped based on their percentile ranking into 4 bins:  $<10^{\text{th}}$ ,  $25^{\text{th}}-50^{\text{th}}$ ,  $50^{\text{th}}-75^{\text{th}}$  and  $>90^{\text{th}}$ . For each trace  $y(t_n)$  the corresponding periodogram

$$|Y(f)|^2 = \frac{\Delta t}{N} \left| \sum_{n=1}^N y(t_n) e^{-ifn} \right|^2 \quad (\text{Equation 12})$$

was calculated. To minimize leakage effects due to the finite time-window of observation, signals were tapered using a triangular window. The power spectrum was finally calculated by averaging periodograms from all traces in each bin. Spectra of simulated time-courses were also included as references, namely 1) pink noise (Bak et al., 1987) and 2) white noise added to a sinusoidal wave

$$y_{\sin}(t_n) = s_1 \sin(2\pi t_n / r_f) + s_2 e \quad (\text{Equation 13})$$

using an independent and identically distributed random variable  $e \in N(0, 1)$ , weighting factors  $s_i$  to adjust the scales, and the reference frequency  $r_f$  of 80 min.

### Mutual Information

To assess the predictability of pulsing classification from the early PC scores, we applied the concept of mutual information (MI). Specifically, the `Mlxnyn` implementation of the MILCA algorithm (Kraskov et al., 2004) was used to determine the MI score between the discretized pulse score (0 = non-pulsing; 1 = pulsing) and the corresponding early fPC scores for each trajectory. MI scores were determined for individual fPC score as well as for combined fPC scores. As reference, we used the entropy of pulsing classification  $H(\text{fp}) = \text{MI}(\text{fp}, \text{fp})$ .

### Fixed-Cell Analysis of ERK-AKT-FoxO3 Connectivity

Data of phosphorylated ERK-T202/Y204 or AKT-S473 and the nuclear translocation of FoxO were collected in 9 cell lines (MCF10A, 184A1, HS578T, BT20, SKBR3, MDA231, MCF7, HCC1806, and T47D) at 8 time points. Several perturbation conditions were measured consisting of stimulation with one of 7 growth factors and no treatment control (8 ligand options), with or without AKT and/or MEK inhibitors (4 inhibitor conditions). This results in a total of 32 perturbation conditions.

Because the activity of endogenous FoxO3 was obtained from different cell populations at different time points, it was not possible to learn a dynamical model directly using measurement at single-cell resolution. We therefore chose quantities representing the characteristics of the population distribution of each measured signal. For the measurement of pERK and pAKT, we chose to use their medians ( $\text{ERK}_\mu$ ,  $\text{AKT}_\mu$ ) as measures of the net level of signal activation at the cell population level. These values were normalized by their maximal values on a per-cell line basis. For FoxO3, we found that perturbations affect both the position (median) and the spreading (inter-quartile range, IQR) of the C/N ratio. We therefore used positions along the curve of FoxO3 C/N translocation ratios in the median vs. IQR landscapes (Figure 7B) as the representative value of FoxO3 activity. In what follows, we will denote this value by  $\text{FoxO3}_\phi$ . With this approach we expect to show a dependence of FoxO3 on ERK and AKT both in terms of its level and its variability (see Figure S9A).

### Quantifying ERK, AKT and FoxO3 Response to Inhibitors

To quantify the effect of MEK inhibition on AKT phosphorylation, we calculated the difference in the median values for AKT,  $AKT_{\mu}$ , at each time point (separately for each combination of cell line and growth factor), in two different inhibitor conditions: with the MEK inhibitor pre-treatment and without any inhibitor pre-treatment (DMSO). This resulted in a vector of difference values across the 8 time points, which we deduced using the corresponding area under the curve. This gives a lumped measure of the overall effect of MEK inhibition on AKT phosphorylation for each cell line/growth factor pair (Figure 7C). To further summarize this effect across all ligand conditions, we took the mean of the AUC values across all ligands to obtain a single representative value for each cell line (red crosses in Figure 7E). Quantification on the effect of AKT inhibition on ERK phosphorylation ( $ERK_{\mu}$ ) was also done in the same manner (Figure 7D and black crosses in Figure 7E). To quantify the effect on FoxO3 by either MEK or AKT inhibition, we used the same AUC-based method but on the position along the parabola in the median vs. IQR landscape ( $FoxO3_{\phi}$ ), as described above.

### Approach to Bayesian Model Comparison

We used the above fixed-cell data from various cell lines to perform Bayesian model discrimination in comparing hypotheses that can best describe the contribution of ERK and AKT activity in FoxO3 translocation. We applied three different dynamic Bayesian network scoring schemes to compare these model hypotheses: two based on a conditionally Gaussian probabilistic model and the third using a discretized approach. From the Bayesian scores obtained from each model we derive probabilities for the support for each individual causal edge between ERK, AKT and FoxO3.

When using the Gaussian-based scoring schemes, we directly used the values described above. For the scoring scheme relying on discrete data, we first performed data discretization as follows. We took data points for each of the 3 variables and independently applied Otsu's discretization technique (Otsu, 1979), which calculates for the optimum threshold such that the intra-class variance is minimized between two groups to which the values are discretized.

### Comparing Model Topologies

We were interested in evaluating causal dependencies representing the relationships between ERK, AKT and FoxO3. We considered four relationships of interest:

1. AKT controlling FoxO3 independent of ERK,
2. ERK controlling FoxO3 independent of AKT,
3. ERK controlling AKT,
4. AKT controlling ERK.

These mechanisms are represented as edges shown in Figure S9B.

We translated these model hypotheses into probabilistic model structures and used Bayesian scoring schemes to quantitatively assess the plausibility of each hypothesis with respect to experimental data. Since there are a total of 4 allowed edges in each model, there are a total of  $2^4=16$  possible overall topologies to consider. Given a data set  $D$  and a set of model topologies  $M_k$ ,  $1 \leq k \leq 16$ , we first calculate the posterior probability of each model,

$$P(M_k|D) = \frac{P(D|M_k)P(M_k)}{P(D)}. \quad (\text{Equation 14})$$

Here  $P(D|M_k)$  is the *marginal likelihood* of model  $M_k$ , and  $P(M_k)$  is the prior probability assigned to the model. We assign equal prior probability to all four models, that is,  $P(M_1) = P(M_2) = \dots = P(M_{16})$ . Consequently, we can calculate the posterior odds of two models as:

$$\frac{P(M_k|D)}{P(M_j|D)} = \frac{P(D|M_k)P(M_k)}{P(D|M_j)P(M_j)} = \frac{P(D|M_k)}{P(D|M_j)}, \quad 1 \leq j \neq k \leq 16. \quad (\text{Equation 15})$$

This shows that models can be compared through their marginal likelihoods. We now turn to the methods for calculation of the marginal likelihood for each model hypothesis. Calculating the marginal likelihood depends on the type of probabilistic model and the assumed parametrization. For model parameters of  $M_k$  summarized in a vector  $\theta_k$ , the marginal likelihood is expressed as

$$P(D|M_k) = \int P(D|M_k, \theta_k)P(\theta_k|M_k)d\theta_k. \quad (\text{Equation 16})$$

A score is thereby assigned to a model by integrating over all possible parametrizations. In many cases the parametrization of the model is such that this integral can be solved analytically (we will consider three such methods), in other cases numerical methods can be used to calculate it. For a general introduction to learning Bayesian networks, we refer the reader to (Neapolitan, 2004).

### Computing Dynamic Bayesian Networks

Assume a network on a set of  $n$  variables  $X = \{X_1, \dots, X_n\}$ . The edges representing the model structure can then be described through the parenthood relationship  $Pa : X \rightarrow 2^X$ . Namely, an edge exists from  $X_i$  to  $X_j$  if and only if  $X_i \in Pa(X_j)$ , with  $1 \leq i, j \leq n$ . The model is

parameterized through a set of conditional probability distributions specifying the distribution of a variable given the value of its parents, or  $P(X_i|Pa(X_i))$ . Through this parenthood relationship, the joint distribution can be written as

$$P(X_1, \dots, X_n) = \prod_{i=1}^n P(X_i|Pa(X_i)). \quad (\text{Equation 17})$$

The above equation shows that the joint distribution of the variables can be derived from the local parenthood structure of each node.

Dynamic Bayesian networks are a special case of Bayesian networks and are used to represent a set of random variables across multiple time points (Murphy, 2002). There are at least two important advantages of using a dynamic Bayesian network compared to static Bayesian network in our setting. First, DBNs allow us to use the available time resolved experimental data directly to learn the model. Second, due to the fact that DBN edges point forward in time, it is possible to model feedback effects (that would normally result in disallowed loops in Bayesian network graphs). Assuming there are a total of  $T$  time points of interest in the process, a DBN will consist of a node representing each of  $n$  variables at each of the  $T$  time points. For instance  $X_i^t$  will denote the  $i$ -th variable at time point  $t$ . Per the standard assumption in the context of DBNs, we assume that the each variable at time  $t$  is independent of all previous variables given the value of its parent variables at time  $t - 1$ . Hence the edges in the network point forward in time and only span a single time step.

We represented as variables the median ( $\mu$ ) of the single-cell measured values of phosphorylated ERK and AKT and the position along the median vs. IQR landscape ( $\phi$ ) of FoxO3 activity at each experimental time point, yielding three random variables. We represented each random variable at each time point where experimental data was available, resulting in a network with a total of 24 random variables. We assume that the structure of the network does not change over time and also that the parameterization is time-invariant. This allows us to use all data for pairs of subsequent time points to score models. Figure S9C shows the DBN representation of one model topology (the topology with all possible edges present). Assuming that the prior probability of each model topology is equal, from these marginal likelihood values, we can calculate the marginal probability of a specific edge  $e$  being present as follows

$$P(e) = \frac{\sum_i [P(M_i|D)|e \in M_i]}{\sum_i P(M_i|D)}. \quad (\text{Equation 18})$$

We applied three different approaches to scoring DBN models and thereby obtaining individual edge probabilities.

### DBN Learning with the BGe Score

In the BGe scoring approach (results shown in Figure S7C) (Geiger and Heckerman, 1994; Grzegorzcyk, 2010) data is assumed to be generated from a conditionally Gaussian distribution with a normal-Wishart prior distribution on the model parameters. The observation is assumed to be distributed as  $N(\mu, \Sigma)$  with the conditional distribution of  $\mu$  defined as  $N(\mu_0, (\nu W)^{-1})$  and the marginal distribution of  $W$  as  $W(\alpha, T_0)$ , that is, a Wishart distribution with  $\alpha$  degrees of freedom and  $T_0$  covariance matrix. We define the hyperparameters of the priors as follows. We set

$$\nu : = 1, \quad \alpha : = n + 2$$

$$\mu_{0j} : = 0, \quad 1 \leq j \leq n,$$

$$T_0 : = \frac{\nu(\alpha - n - 1)}{\nu + 1} I_{n,n},$$

where  $n$  is the total number of modeled species. The marginal likelihood of a model for a subset of the data  $D'$  on  $n'$  nodes with these assumptions can be expressed as follows.

$$P(D'|M_k) = (2\pi)^{-n'/m/2} \cdot \left(\frac{\nu}{\nu+m}\right)^{n'/2} \cdot \frac{c(n', \alpha)}{c(n', \alpha+m)} \cdot \det(T_0)^{\alpha/2} \cdot \det(T_{D',m})^{-(\alpha+m)/2}, \quad (\text{Equation 19})$$

with

$$T_{D',m} = D_0 + (m-1) \cdot \text{Cov}(D) + \frac{\nu m}{\nu+m} (\mu_0 - \bar{D})(\mu_0 - \bar{D})^T, \quad (\text{Equation 20})$$

and

$$c(n, \alpha) = \left( 2^{\alpha n/2} \cdot \pi^{n(n-1)/4} \prod_{i=1}^n \Gamma\left(\frac{\alpha+1-i}{2}\right) \right)^{-1}. \quad (\text{Equation 21})$$

The full marginal likelihood is then calculated as

$$P(D|M_k) = \prod_{i=1}^n \frac{P(D^{i,\pi_i}|M_k)}{P(D^{\pi_i}|M_k)}, \quad (\text{Equation 22})$$

where  $D^{i,\pi_i}$  denotes the subset of the data for the  $i$ -th node and its parents and  $D^{\pi_i}$  the subset of data for the  $i$ -th node's parents only. Note that these subsets of data are constructed such that the data for the  $i$ -th node is shifted forward by one time-step to align with the parents' data.

### DBN Learning with g-prior Based Gaussian Score

We adapted the DBN learning approach developed by Hill et al. (results shown in Figure 7F) (Hill et al., 2012). This approach is similar to the BGe approach in that it assumes a conditional Gaussian probability distribution for the variables in the model. It, however, chooses a different prior parametrization leading to desirable properties including the fact that parameters don't need to be user-set and that the score is invariant to data rescaling. One shortcoming of this method is that it requires matrix inversion and is therefore prone to conditioning problems. Here we only present the formula for the marginal likelihood calculation and refer to Hill et al. (2012) for the details of the conditional probability model. The formula for calculating the marginal likelihood for node  $i$  is

$$P(D_i|M_k) = (1+m)^{-(2^{|\pi_i|-1})/2} \left( D_i^T D_i - \frac{m}{m+1} D_i^T B_i (B_i^T B_i)^{-1} B_i^T D_i \right)^{-m/2}, \quad (\text{Equation 23})$$

where  $D_i$  is the subset of the data for the  $i$ -th variable, shifted forward by one time step,  $B_i$  is a design matrix containing the data for the  $i$ -th node's parents and possibly the higher order products of the parents' data to model upstream interactions. We do not use higher order interaction terms in the current study. The full marginal likelihood is expressed as

$$P(D|M_k) = \prod_{i=1}^n P(D_i|M_k). \quad (\text{Equation 24})$$

### DBN Learning with the BDe Score

The BDe scoring metric (results shown in Figure S7D) (Friedman et al., 1998; Heckerman et al., 1995) relies on the assumption that each random variable is binary, that is,  $X_i \in \{0, 1\}$ . Consequently, the model is parametrized by a set of conditional probability tables containing the probabilities that a node takes the value 1 given all possible combinations of values assigned to its parents. For instance, in a specific topology, the conditional probability table of FoxO3a $\phi^t = v_1$  | AKT $\mu^{t-1} = v_2$  for all combinations of  $v_1, v_2 \in \{0, 1\}$ . Note that the conditional probability distributions have to sum to one, that is,  $\sum_{v_1 \in \{0,1\}} P(\text{Foxo3a}\phi^t = v_1 | \text{AKT}\mu^t = v_2) = 1$ .

The BDe score assumes a beta distribution as the prior for the model parameters. Using beta priors, Heckerman et al. (1995) shows that the marginal likelihood can be expressed as

$$P(D|M_k) = \prod_{i=1}^n \prod_{j=1}^{q_i} \frac{\Gamma(s_{ij})}{\Gamma(d_{ij} + s_{ij})} \prod_{\ell \in \{0,1\}} \frac{\Gamma(d_{ij\ell} + s_{ij\ell})}{\Gamma(s_{ij\ell})}, \quad (\text{Equation 25})$$

where  $i$  refers to a node  $X_i$ ,  $j$  is a value configuration of the parents of node  $X_i$ , with  $q_i$  the total number of parent value configurations, and  $\ell$  indicates the value of node  $X_i$  under parent configuration  $j$ . For each combination of indices,  $d_{ij}$  and  $d_{ij\ell}$  represent the observed count, while  $s_{ij}$  and  $s_{ij\ell}$  are the prior counts. To make priors consistent among different DAG structures, we choose a fix equivalent sample size  $S = 1$ , and set  $s_{ij\ell} = S/(2q_i)$ . For instance, assume we want to score the model  $M_1$ , and that we denote  $X_3 = \text{AKT}\mu$  and  $X_5 = \text{FoxO3}\mu$ , with which  $Pa(X_5) = \{X_3\}$ , and  $q_5 = 2$ . Then, for instance,  $d_{510}$  is the number of experiments in which AKT $\mu$  takes the value 0 and FoxO3 $\mu$  takes the value 0. Similarly,  $d_{511}$  corresponds to the number of experiments in which AKT $\mu$  takes the value 0.

### DATA AND SOFTWARE AVAILABILITY

Raw images and LINCS-compatible CSV datasets can be accessed at <http://lincs.hms.harvard.edu/sampattavanich-cellsyst-2018/>.

Extracted data in other formats are available at <https://doi.org/10.17632/65fdzt9x5.1>.

Scripts used to generate all figures are available at <https://github.com/sorgerlab/sampattavanich-cellsyst-2018>.